FINAL REPORT FOR: AFOSR GRANT F49260-02-1-0284

TRANSONIC CASCADE MEASUREMENTS TO SUPPORT ANALYTICAL MODELING

Paul A. Durbin, John K. Eaton, Greg Laskowski, and Amanda Vicharelli

Department of Mechanical Engineering
Stanford University
Stanford CA 94305-3030
Tel.: 650-723-9311 (PAD); 650-723-1971 (JKE)
durbin@vk.stanford.edu; eaton@vk.stanford.edu

submitted to:

Attn: Dr. John Schmisseur
Air Force Office of Scientific Research
875 N. Randolph Street
Suite 325, Room 3112
Arlington, VA 22203

Grant start date: 1 June 2002
Grant end date: 30 November 2004
Date of submission: 17 May 2005

Abstract

Turbulence measurements were made in a transonic turbine cascade using PIV in a unique two-passage model consisting of a single full blade and two shaped outer walls. The outer wall shapes were prescribed using an inverse design procedure that gave the correct infinite-cascade pressure and mean velocity distribution around the blade. The outer surfaces of the curved walls were shaped to steer a laser sheet to provide uniform illumination for the PIV. The PIV measurements were performed over a large number of small domains providing excellent spatial resolution over most of the flowfield. Measurements in the freestream above the blade boundary layers showed that the absolute magnitude of the turbulent stresses changed little through the strong acceleration and curvature. This means that the relative turbulence intensity falls rapidly as the flow accelerates through the cascade. Detailed comparison to various turbulence models is underway.

Preface

A follow on grant has been funded to continue these cascade measurements and to use the two-passage rig to initiate a study of trailing edge cooling flows. We report herein the accomplishments of the initial grant period, and current work in progress. In addition to the technical material, we report that Greg Laskowski completed his PhD in the Aero-Astro department, with partial support of this program, and Amanda Vicharelli completed her MS in Aero-Astro, with full support from this program. Amanda is continuing to work on the project as a PhD student.

1 Introduction

A major limiting factor affecting the performance and life of gas-turbine based aircraft propulsion systems is the high metal temperatures of high pressure turbine components. The emphasis in advanced engine design is to use the available cooling air in the most effective way possible, to produce a desired blade metal temperature distribution that minimizes thermal stresses while avoiding high temperature corrosion. Extensive prototype testing is used to achieve the desired cooling performance, a process that is expensive, time consuming, and does not yield an optimal solution. Accurate and robust methods are needed to calculate the turbine blade temperature distribution over a range of operating conditions. An important pacing item is the development of models capable of accurately computing the heat transfer coefficient and film cooling effectiveness on the blade surface. A major issue is modeling the effects of freestream turbulence on the blade heat transfer. Previous research has investigated the effect of high turbulence levels on heat transfer in boundary layers and near stagnation lines. What is not known is how the freestream turbulence varies through the turbine passage. Intuition suggests that the relative turbulence intensity would drop rapidly, but most models predict rapid increases in the turbulent stresses, a well known failing of turbulence models in flows

REPORT DOCUMENTATION PAGE

AFRL-SR-AR-TR-05-

O2b3

The public reporting burden for this collection of information is estimated to average 1 hour per response, including the tim gathering and maintaining the data needed, and completing and reviewing the collection of information. Send comments rega of information, including suggestions for reducing the burden, to Department of Defense, Washington Headquarters S (0704-0188), 1215 Jefferson Davis Highway, Suite 1204, Arlington, VA 22202-4302. Respondents should be aware that notwithstanding any other provision subject to any penalty for failing to comply with a collection of information if it does not display a currently valid OMB control number.
PLEASE DO NOT RETURN YOUR FORM TO THE ABOVE ADDRESS.

1. REPORT DATE (DD-MM-YYYY)	2. REPORT TYPE	3. DATES COVERED (From - To)
17052005	Final Report	01 Jun 2002 - 30 Sep 2004

4. TITLE AND SUBTITLE	5a. CONTRACT NUMBER
Transonic Cascade Measurements to Support Analytical Modeling	
	5b. GRANT NUMBER
	F49620-02-1-0284
	5c. PROGRAM ELEMENT NUMBER

6. AUTHOR(S)	5d. PROJECT NUMBER
John K Eaton	
	5e. TASK NUMBER
	5f. WORK UNIT NUMBER

7. PERFORMING ORGANIZATION NAME(S) AND ADDRESS(ES)	8. PERFORMING ORGANIZATION REPORT NUMBER
Department of Mechanical Engineering Stanford University Stanford CA 94305-3030 NA	

9. SPONSORING/MONITORING AGENCY NAME(S) AND ADDRESS(ES)	10. SPONSOR/MONITOR'S ACRONYM(S)
USAF/AFRL AFOSR 875 North Randolph Street Arlington VA 22203	
	11. SPONSOR/MONITOR'S REPORT NUMBER(S)

12. DISTRIBUTION/AVAILABILITY STATEMENT

Distribution Statement A. Approved for public release; distribution is unlimited.

13. SUPPLEMENTARY NOTES

14. ABSTRACT

Turbulence measurements were made in a transonic turbine cascade using PIV in a unique two-passage model consisting of a single full blade and two shaped outer walls. The outer wall shapes were prescribed using an inverse design procedure that gave the correct infinite-cascade pressure and mean velocity distribution around the blade. The outer surfaces of the curved walls were shaped to steer a laser sheet to provide uniform illumination for the PIV. The PIV measurements were performed over a large number of small domains providing excellent spatial resolution over most of the flowfield. Measurements in the freestream above the blade boundary layers showed that the absolute magnitude of the turbulent stresses changed little through the strong acceleration and curvature. This means that the relative turbulence intensity falls rapidly as the flow accelerates through the cascade. Detailed comparison to various turbulence models is underway.

15. SUBJECT TERMS

16. SECURITY CLASSIFICATION OF:			17. LIMITATION OF ABSTRACT	18. NUMBER OF PAGES	19a. NAME OF RESPONSIBLE PERSON
a. REPORT	b. ABSTRACT	c. THIS PAGE			
U	U	U	UU	40	19b. TELEPHONE NUMBER (Include area code)

7-7-05

containing regions of strong irrotational strain. Some models place a limit on either the turbulent time scale or the rate of energy production to avoid excessive levels of turbulent kinetic energy. However, these models have not been tested extensively against well-qualified data in the turbine environment.

The objective of this program is to provide a detailed set of turbulence measurements in a transonic turbine cascade that captures much of the complexity of a real turbine stage but still provides high measurement resolution and well controlled boundary conditions for comparison to computational techniques. Typical methods of constructing linear cascades are not appropriate for our purpose since the bleeds and tailboards that are most often used to adjust the flow conditions would interfere with both the optical access and the accuracy of future comparisons to CFD. The alternate approach of using a large number of blades to create an effective periodic flow around the central blade is also not feasible due to the limited output of our compressor. Rather than attempting to modify the existing techniques we instead developed a new method for designing cascade experiments. Our approach uses an inverse-design procedure to shape two outer walls around a single blade in order to reproduce the mean flow of an infinite turbine cascade. Using this technique we are able to accurately represent a high pressure turbine flow at a single design condition, in a wind tunnel with a relatively simple geometry. The cascade is operated at realistic Mach and Reynolds number with moderately high inlet freestream turbulence. Measurements are obtained using a high-resolution 2-D PIV system. This report first describes the inverse design procedure which is a useful product of the research on its own, then presents the PIV measurements obtained around the blade.

2 Cascade Design Methodology

2.1 Inverse Problem Definition

In order to design the passage walls such that the flow in the double passage was representative of the flow in an infinite cascade, it was necessary to define a cost function that was also representative of the overall flow field. In doing so we followed the practice used in airfoil design, and initially decided to match the surface pressure in the form of Surface Isentropic Mach Number (SIMN) of the blade in the passage to that of the blade in an infinite cascade. Thus the design optimization problem statement is:

$$\min_{\phi}\left\{j(\phi, \mathbf{U}(\phi)) : \mathbf{E}(\phi, \mathbf{U}(\phi)) = 0\right\} \tag{1}$$

where j is the cost function, ϕ are the control variables, $\mathbf{U}$ is the state variable vector, and $\mathbf{E}$ is the set of governing equations to be solved. The global cost function is defined as:

$$j = \sum_{i=1}^{I} \alpha_i \gamma_i(\mathbf{U}) \tag{2}$$

3

where α is a set of weights to be determined heuristically, I is the number of cost function components constituting the global cost function, and γ_i are the cost function components. Initially I was taken to be 1, α_1 was set to 1, and γ_1 was defined as:

$$\gamma_1 = \int_{\Gamma_{blade}} \beta(s)|M - M^*|ds \qquad (3)$$

Here $\beta(s)$ is a step-function scaling factor, M is the SIMN distribution (double passage), and M^* is the target SIMN distribution (infinite cascade), with the isentropic Mach number defined as:

$$M = \sqrt{\frac{2}{\gamma-1}\left[\left(\frac{P_t}{P}\right)^{\frac{\gamma-1}{\gamma}} - 1\right]} \qquad (4)$$

where P_t is the stagnation pressure, P is the static pressure and γ is the ratio of specific heats, which is taken to be 1.4 for air.

The cost function was minimized by the method of steepest descent. The control variable ϕ in (1) is updated as:

$$\phi_i^{k+1} = \phi_i^k - c\nabla j\left(\phi_i^k\right) \qquad (5)$$

until the minimum of (2) is achieved. In (5), c is the step size which was either held constant or computed using a line search based on a parabola fit. The latter is analogous to a response surface method. A simple backward difference was used for the gradient computations:

$$\nabla j\left(\phi_i^k\right) = \frac{j\left(\phi_i^k + \Delta\right) - j\left(\phi_i^k\right)}{\Delta} \qquad (6)$$

where Δ represents a perturbation to the control variable.

Since the objective was to shape the passage walls in order to achieve the correct SIMN distribution along the blade, a natural choice for the control variables was a set of spline points used to construct the wall shapes. The initial wall geometry and spline point positioning will be shown in the Results section. In order to keep the number of degrees of freedom to a minimum, cylindrical coordinates were used with the origin placed at the leading edge of the blade and only the radial location of the control points was varied. Thus:

$$\phi = \phi(r, \theta = \text{const.})$$

Once the control points were moved, either due to a perturbation or due to a gradient update, a piecewise cubic spline was fit through the points.

2.2 Implementation

Since the viscous boundary layers are critically important, the Favre-averaged Navier-Stokes equations were solved with the Chen two-layer k-ε model in order to determine the flow field in the passage. The two-equation Chen k-ε model [1] was selected based on the turbulence model assessment of [2] to compute μ_T. The model does not account for transition, and the boundary layer that develops along the passage walls and blade surface is assumed to be turbulent which follows the work of [2]. The two-layer model was used along the blade surface and wall functions were used along passage walls. The governing equations were solved using STAR-CD, a finite-volume commercial CFD package developed by Adapco [1]. The SIMPLE algorithm with 2nd order Monotone Advection Residual Scheme (MARS) for the spatial flux computations was used.

Figure 1 shows the computational grid used for the simulation of the infinite cascade. The O-grid consisted of 180 points in the circumferential direction, with 51 points in the transverse direction. The inlet and the exit of the O-grid were extended with an H-grid. Sixteen grid points were used for the entrance section while 24 points were used for the exit section. The maximum value of y^+ for the nearest grid point to the blade was 0.9.

Stagnation pressure and temperature corresponding to the values in Table 1, as well as the direction cosine (0.488,0.873), turbulence intensity (5%) and turbulent length scale (0.001 m) were set at the inflow boundary to coincide with the experiment. The static pressure was set to atmospheric at the outflow boundary with a zero gradient boundary condition for turbulence quantities and temperature. Periodic boundary conditions were set at the upper and lower boundary, along the mid-pitch line. Finally adiabatic no-slip with two-layer k-ε was invoked at the blade surface. Convergence was achieved when all residuals dropped at least 8 orders in magnitude.

The grid used in the infinite cascade simulation was modified for use in the double passage simulation. Grid refinement studies showed that at least 70,000 cells were required for the simulations. The same inflow and outflow conditions as those used in the infinite cascade simulation were used and the inflow conditions coincide with the experiment. No-slip adiabatic wall with the two-layer k-ε model was specified at the blade surface, whereas adiabatic walls with wall functions were used for the passage walls. This was done in order to keep the number of grid cells to a minimum, and it was determined that wall functions along the passage walls did not degrade the overall results. The grid was constructed, and the results were monitored, to ensure that all values of y^+ for the nearest cell to the blade surface were well within the viscous sub-layer, and within the log-layer along the passage walls.

2.3 Algorithm

First the infinite cascade simulation for the blade was conducted at transonic conditions. The SIMN and stagnation streamlines were extracted, the former to be used as the initial cost function definition, and the latter to be used as the initial guess for the wall shapes. Once the stagnation streamlines were offset by the pitch, a set of points was extracted to be used as both spline and control points for subsequent wall shape definitions. An algebraic grid generator was used to generate the grid for the blade-wall geometry and the CFD simulation was run until convergence was achieved. A script controlling the perturbations, spline fits, grid generation, flow field computations and cost function evaluations was written to loop sequentially through the control points for each global iteration.

During the optimization it became clear that modifying the suction wall had no discernable effect on the pressure-side pressure distribution, and vice versa. As such, the two walls were optimized simultaneously and independently for different definitions of Eq. 3. Furthermore, it was observed that the pressure wall needed to be divided into two distinct sections, a subsonic region upstream of the throat, and a downstream supersonic region. Thus, Eq. 3 takes the form:

$$\gamma_{M<1} = \beta_1 \int_{\Gamma_{inlet \to throat}} |M - M^*| ds + \beta_2 \int_{\Gamma_{throat}} |M - M^*| ds$$

$$\gamma_{M>1} = \beta_2 \int_{\Gamma_{throat}} |M - M^*| ds + \beta_3 \int_{\Gamma_{throat \to exit}} |M - M^*| ds$$

where :

$$\beta_2 >> \beta_1 \quad \& \quad \beta_2 >> \beta_3$$

Furthermore, the step size in Eq. 5 was held fixed.

The wind tunnel components supporting the passage were constructed concurrently with the optimization process, and several design iterations for the wall shape were built and tested in order to refine and improve the technique. The first and the final wall designs will be presented here, along with the corresponding modifications to the cost function.

3 Experimental Methods

3.1 Double Passage

The experimental apparatus was designed around the optimized geometry to adapt it to an existing wind tunnel while maximizing the optical access to the blade. The individual rig components were designed so that the passage walls could be replaced with walls of a different shape, allowing for an iterative approach for the design optimization. The passage geometry can be seen in the test section schematic in Figure 2. The two-dimensional passage is formed between two parallel aluminum plates in the plane of the

figure with a spacing of approximately 1 chord length. The passage walls were CNC machined out of transparent Plexiglas to the internal shape prescribed by the CFD optimization. The inner wall shape generated by the optimization procedure consisted of nearly 200 coordinate points for each wall surface. These two sets of points were fitted manually with NURBS splines and converted into machine motion using Mastercam (Mill V9). The external wall shape was designed separately to give the wall the correct optical properties for transmission of the PIV light sheet, and the minimum wall thickness was set to 12.7 mm to ensure rigidity. The two-dimensional wall shape was converted to machine motion with a linearization tolerance of 0.25 µm to ensure high accuracy of the machined shape, and the resulting G-code used 28,000 steps for each pass around the surface. The wall surfaces were cut with five passes in the approach plane and eight passes in depth to minimize tool deflection. The machined surfaces were mechanically polished to high transparency using plastic polish (Meguiar's Clear Plastic Polish #10) and a layered fabric buffing wheel. To seal the connection between the walls and the aluminum end plates a 1.6 mm O-ring groove was cut parallel to the inner wall surface on both sides of each plastic part. In addition steel alignment pins were press-fit into the sides of each part, and they mate with matching holes in the aluminum endwalls to lock the walls in the correct location with respect to the central blade. The transparent passage walls are clamped between the two end plates with a set of bolts running in the spanwise direction.

The solid stainless steel blade was cut with Electrical Discharge Machining (wire EDM) and it fits into an identically shaped EDM-cut slot in one of the two aluminum endwalls. RTV sealant was used to fill the ~15 µm clearance between the blade and its matching endwall slot. The opposite endwall includes two windows for PIV imaging. The two 12.7 mm thick optical-quality glass windows fit into machined pockets flush with the endwall surface. The window joints are sealed with O-rings which also serve to lock the windows in place between the passage walls and the aluminum end plate. On the window side of the inside passage the steel blade sits flush with the glass, where it is sealed and cushioned with a thin layer of RTV sealant. A screw with a nylon bushing threads through a hole in the glass window and into the steel blade to reinforce the seal at the blade-window interface. O-rings provide sealing at all flange connections.

The blade was equipped with 17 static pressure taps. Holes with a diameter of 0.58 mm were drilled perpendicular to the blade surface mid-span and were connected to a Scanivalve (model SSS-48C-MK4) through vinyl tubes extending out the far endwall. The blade surface pressure was measured relative to the flow stagnation pressure at the cascade inlet using a Kiel probe and a Setra model 204D pressure transducer. The Kiel probe was also connected to a Bourdon tube manometer (Wallace & Tiernan FA 145), to ensure that the inlet stagnation pressure in the passage matched that of the infinite cascade, and to double-check the transducer calibration. Voltage signals were acquired using a National Instruments PC-MIO-16E-4 board and controlled using LabVIEW software. The resulting pressure measurements were then used to calculate the SIMN distribution using Eq. 4.

3.2 Overall Wind Tunnel System

A schematic of the upstream wind tunnel components is shown in Figure 3. Flow is provided by an Ingersoll-Rand compressor (SSR-XF400), which provides a continuous flow of 0.64 kg/sec at 5.7×10^5 Pa. Upstream of the test section the flow passes through an air filter (F18-C00-A3DA) followed by a regulator (Norgren R18-C05-RNSA) which is used to control the total pressure in the test section. After the regulator, the flow passes through a heat exchanger (CMS Heat Transfer Division, Inc.) which uses a variable supply of chilled water to keep the test section temperature constant at 295 K. Following the heat exchanger the flow passes through a corner-flange orifice plate. The mass flow rate is determined from the pressure drop across the orifice plate.

The flow develops in a 1.5 m long duct with an 86.4 by 14.3 mm cross section. This development duct includes three honeycomb sections (51 mm long by 6 mm cell size) as well as six 1.6 mm thick circular-hole grids (47% - 52% blockage) to produce uniform flow at entrance to the contraction. The three-dimensional nozzle at the entrance to the test section has a 4.6:1 area contraction ratio reducing the passage size to the 42.3 by 50.8 mm dimensions of the test section inlet. Wall contours in both contracting directions were designed using 5th order polynomials with zero first and second derivatives at the inlet and outlet to insure thin boundary layers at the test section inlet. A removable grid could be installed just upstream of the contraction. This grid produced freestream turbulence levels in excess of 14% upstream of the contraction. The contraction reduced the turbulence intensity to approximately 5% at the test section inlet. Detailed documentation of the inlet state is provided in the Results section. After passing through the turbine passage the flow exhausts into a large plenum chamber, which is adapted to a muffler that exhausts to atmosphere allowing for supersonic flow in the passage.

The total pressure in the test section was measured with a Kiel probe positioned at midspan 32 mm downstream of the passage inlet, and was monitored for the duration of each experiment using a Bourdon tube manometer (Wallace & Tiernan FA 145) and a Setra 204D (0-5.7 x 10^5 Pa) pressure transducer. (For the upstream PIV measurements the probe was moved to a second port, 70 mm downstream of the inlet). The temperature was measured upstream of the contraction using an Omega 44004 thermistor. The overall geometry and flow conditions used in this experiment are outlined in Table 1.

3.3 PIV Setup

The mean velocity and turbulence quantities were measured using two-dimensional digital particle image velocimetry (PIV). Two difficulties that must be addressed when PIV is applied to transonic flows are that the seed particles need to be very small to minimize the velocity lag, and they need to be provided in large quantities and distributed evenly to ensure adequate particle density in the PIV images. The screw type compressor supplying the flow injects a small amount of oil vapor into the air stream. As the pressure drops through the pressure regulator and upstream tunnel components the oil condenses into very small droplets. The tracer particles were initially estimated to be < 1 μm in diameter based on visual inspection of the particle images of tracer particles

compared to the nominally 1 μm droplets generated by a well-documented TSI oil droplet generator. PIV measurements obtained at the trailing edge shock confirm that the particle lag time is negligible at the resolution of the measurements. Figure 4 shows both the mean velocity and a single instantaneous profile taken from a PIV measurement window that spans the trailing edge shock. The plot is dimensional to show the scale of the measurements and the shock strength. The shock appears to have a thickness of about 1mm in the mean profile, but this is caused by unsteadiness in the shock position rather than particle lag effects. The instantaneous profile shows that the particles are able to respond to the shock to the limit of the measurement resolution of 190 μm, indicating that the particle recovery curve occurs over a distance that is smaller than the grid resolution. Therefore an upper bound for the particle time constant can be estimated as the time it takes a fluid element to move from one grid point to the next. The particle time constant based on the grid spacing and flow velocity before the shock is 0.47 μs, corresponding to a particle diameter of 0.40 μm. This is an upper limit only; while the true particle size is likely to be much smaller, any difference in size below 0.40 μm will not be reflected in the measured result due to the spatial averaging performed in the PIV analysis.

Because of the small size of the tracer droplets, an intense illumination sheet is required. A double pulsed Nd:Yag laser (Spectra Physics PIV-400) was used for this purpose. The laser generates a maximum energy of about 350 mJ per 10 ns pulse at a wavelength of 532 nm. Two mirrors were used to direct the beam to the laser sheet optics, which consist of a cylindrical lens and a spherical lens with focal lengths of −50 mm and 500 mm respectively. The resulting light sheet had a thickness of approximately 120 μm at the waist. The optics were positioned for each measurement set so that the sheet enters the passage through the Plexiglas sidewall at midspan, parallel to the passage geometry, with the sheet waist at the region of interest in the passage.

Images were acquired using a TSI camera (PIVCAM13-8) and TSI frame grabber. The 12-bit, 1024 by 1280 pixel CCD camera was capable of acquiring image pairs with a minimum time delay of 0.5 μs between images. The camera was used with a Nikkor 200 mm lens at f/4 and was oriented perpendicular to the light sheet. Timing signals for the laser pulsing and camera exposure were controlled with a TSI LaserPulse synchronizer (model 610034), which was connected to a Dell workstation equipped with TSI Insight software. Image pairs were acquired at a nominal rate of 1 Hz. A schematic of the PIV system and optics setup is shown in Fig. 3.

PIV measurements were calibrated using a black-anodized aluminum plate etched with the test section geometry and a superimposed grid. A calibration image was obtained for each measurement set by removing the test section from the wind tunnel and positioning the calibration plate in the spanwise location of the light sheet. This image was used to determine the magnification of the imaging system and the location of each measurement window. A single aluminum endwall with identical glass windows to the ones in the test section was installed in the correct location to duplicate the optical distortion caused by the test section windows.

3.4 PIV Measurements

In order to achieve the highest possible spatial resolution, data were taken in several small windows and then combined into a single set. The maximum possible magnification was limited by the available seeding density, (ie minimum of 5 particles needed per 32 x 32 pixel interrogation region). The high seeding density allowed for magnifications of about 12 μm/pixel, corresponding to a measurement window size of 12 x 15 mm. The laser time delay was selected to create the largest possible particle displacement as allowed for PIV processing. Smaller particle displacements can give accurate mean velocity results, but larger displacements are needed to accurately measure the fluctuating velocities. The maximum permissible time delay was limited by the particles leaving the light sheet, particles leaving the image window, and high local velocity gradients (distortions in the particle pattern) due to freestream turbulence. For these reasons the optimal time delay was different for each measurement window, and was between 0.8 and 7.2 μs depending on the spatial mean velocity within the measurement window.

A total of 34 measurement windows were used to cover the passage in the upstream region and in the area around the blade. Some overlap of the windows was required since valid measurements only covered the center of each window due to light sheet positioning and particles leaving the image. A map showing all of the measurement windows is shown in Fig. 5. Because of the glare that occurs where the light sheet hits a wall it was only possible to collect useful data to within 1-2 mm of the wall and blade surfaces.

Since the overall geometry is relatively small, care was required to aim the light sheet to cover only the region of interest. In addition the highly curved inner wall shape caused significant optical distortion of the light sheet, so that in some areas it would be nearly impossible to obtain uniform lighting in the correct position in the passage. To correct for this, the outer wall shape was designed using a custom ray-tracing program to counteract the optical distortion caused by the curved inner wall surface. Figure 6 shows an illustration of the wall shape used to create optical access to the supersonic region on the suction side of the blade. The ray tracing program was also used to calculate the best way to position the sheet optics for illuminating each measurement window. Even with these measures, some regions of the flow could not be imaged, such as the region inside the pressure side of the highly cambered blade surface.

3.5 PIV Processing

In two dimensional cross-correlation PIV, small interrogation regions are cross correlated in two consecutive images to determine the average displacement of particles in each interrogation region (IR). Since this experiment contains a highly turbulent accelerating flow, there were both high mean velocity gradients within each measurement window and high local velocity gradients within each IR. Custom software was used to calculate the optimal offset for each IR, using the iterative technique proposed by Westerweel [3]. The software used was a modified version of the code written by Han [4]. First an initial

approximation for the displacement field was calculated from a CFD calculation or low turbulence measurements and applied to a coarse (64 x 64 pixel) grid. A first cross-correlation was performed using this initial offset on the coarse grid, and the resulting displacement was used as the initial offset for a second calculation of the cross-correlation. The resulting offset was then interpolated onto a finer (32 x 32 pixel) grid, and five more iterations were performed on the 32 x 32 pixel grid with the range decreasing at each iteration to fine-tune the result. This iterative technique eliminates the need for small pixel displacements and it also eliminates the bias towards low velocity values associated with the FFT algorithm used to calculate the correlations. This processing technique allowed for measurement displacements in the range of 20-50 pixels, increasing the measurement accuracy. Between iterations, erroneous vectors were filtered out using a consistency filter and replaced with interpolated vectors. At the final iteration, spurious vectors were marked and interpolated vectors were not included in the final result. An example of a validated vector field calculated from a single image pair is shown in Fig. 7.

To obtain accurate turbulence statistics, 3000 image pairs were taken at each measurement location. Typically 95-98% of the vectors at any given location were used for each measurement window. The final interrogation region size of 32 pixels used with 50% overlap created a 55 by 71 vector grid for each measurement window, with a spatial resolution of about 190 um.

The validated vector fields were ensemble averaged to obtain the two dimensional mean and fluctuating velocities in each measurement window. The resulting statistical data were cropped to include only the portion in the passage that was illuminated by the light sheet, as shown in Fig. 7, and interpolated onto a single grid with 200 μm spacing. Data were averaged in regions with overlap, and in most regions 20-30% of each data set was overlapped with other data. Additional approximations were made to calculate the turbulent kinetic energy and dissipation rate. The turbulent kinetic energy was approximated as

$$k \approx \tfrac{3}{4}\left(u'^2 + v'^2\right)$$
(7)

and the local turbulence intensity was calculated as

$$Tu = \sqrt{\tfrac{2}{3}k} / \sqrt{\left(U^2 + V^2\right)}$$
(8)

The instantaneous vector fields were used to approximate the dissipation rate in each measurement window using the large-eddy PIV method described by Sheng et al [5]. PIV measurements present the opportunity to calculate the dissipation rate directly using the spatially resolved instantaneous velocity field. Since the measured velocity at each point represents a spatial average over each interrogation region, the results are effectively low-pass filtered in a way that is similar to large eddy simulation (LES). The large-eddy PIV method borrows the concept from LES that the turbulent kinetic energy dissipation rate can be calculated as the energy flux from the resolved scale (in this case,

the size of the IR) to the unresolved scales, if the flow can be assumed to be in dynamic equilibrium and the filter scale is in the inertial subrange. The filtered Reynolds averaged Navier-Stokes equations provide the sub-grid scale (SGS) dissipation rate:

$$\varepsilon = -2 < \tau_{ij} S_{ij} >$$ (9)

Where S_{ij} is the resolved instantaneous strain rate tensor,

$$S_{ij} = \frac{1}{2} \left(\frac{\partial u_i}{\partial x_j} + \frac{\partial u_j}{\partial x_i} \right)$$ (10)

and τ_{ij} is the SGS stress tensor,

$$\tau_{ij} = \overline{u_i u_j} - \overline{u}_i \overline{u}_j$$ (11)

which must be modeled.

The Smagorinsky model was used for this calculation:

$$\tau_{ij} = -C_s{}^2 \Delta^2 |S| S_{ij}$$ (12)

where Δ is the filter size (in this case 32 pix $\approx$ 380µm), and $C_s = 0.17$ is the Smagorinsky constant. Here the lowercase u represents the instantaneous velocity, the bar indicates a spatial average over the filter size, and the <>'s indicate a time average (in this case an ensemble average over the 3000 vector fields for each measurement window). Since only four components of the velocity gradient tensor were measured by the PIV, the missing diagonal component was approximated from continuity (neglecting compressibility) and the remaining off-diagonal terms were assumed to be equal to the measured off-diagonal term. Raw vector fields were used with central differencing to calculate the dissipation field for each image pair in each measurement window. Results at a single point were neglected if any of the four points used in the derivative calculations were marked as invalid during the PIV image processing. The resulting validated dissipation fields were then ensemble averaged and interpolated onto a single grid, with the values averaged in regions of overlap.

Uncertainty estimates were different for different regions of the flow due to an intermittent separation observed in the corner of the pressure surface above the blade. This was seen as a bimodal velocity probability density function for the instantaneous velocity at positions near the corner. It also appears in the turbulence statistics as a highly turbulent streak that originates in the corner and convects downstream in the top of the upper passage. A very large number of samples would be required to accurately represent the turbulence associated with the low frequency shedding of the corner boundary layer. For this reason a higher level of statistical uncertainty was accepted for the upper passage. The statistical uncertainty in U and V is between ± 0.1 and 0.2 m/s in most of the passage, which corresponds to 0.04% to 0.2% of the local flow velocity

depending on the location. In the upper passage region with the turbulent streak, the velocity uncertainty is up to ± 0.8 m/s. The uncertainty in u'^2 is between 0.51 and 2.50 m^2/s^2 in most of the passage, and the uncertainty in v'^2 is between 0.63 and 3.50 m^2/s^2 in most of the passage. In the upper passage the uncertainty in u'^2 is up to ± 20 m^2/s^2, while the uncertainty in v'^2 is up to ± 48 m^2/s^2 in the corner region and up to ± 26 m^2/s^2 in the upper passage. The uncertainty in the stresses is also higher in the blade wake and trailing edge shocks, up to ± 40 m^2/s^2 for u'^2 and ± 50 m^2/s^2 for v'^2. However, when the stress uncertainty is normalized by the local values it is between 2.3% and 5.6% everywhere.

The displacement uncertainty for the PIV measurements was estimated as ± 0.2 pixels, which corresponds to a velocity uncertainty of ± 0.4 - 3.2 m/s, or 0.3 - 1.7% of the local flow velocity. The uncertainty in the dissipation rate calculation was estimated by analyzing upstream PIV measurements for two different measurement resolutions. The sensitivity of the LES model was estimated by calculating the results as a function of the grid spacing used for the derivative calculations, and the accuracy of the inertial subrange assumption was assessed by calculating the dissipation rate directly for different grid spacings and measurement resolutions. In addition the error due to measurement noise was estimated by inserting the 0.2 pixel measurement uncertainty directly into the dissipation equations, and the values obtained for the upstream dissipation rate were compared to the kinetic energy decay rate measured in the upstream passage. Overall the dissipation rate uncertainty was estimated at 50% of the local values. Detailed explanation of the uncertainty analysis can be found in [6].

4   Results: Cascade Development and Design Validation

4.1 Initial Design

Figure 8 shows the initial geometry that was used in the optimization, based on the stagnation streamline from the infinite cascade solution offset by one pitch in either direction. The streamlines were fitted with splines and linear extensions were applied at the ends to form the entrance and exit ducts. Also shown in the figure are the spline points and control points used in the optimization. Figure 9 shows the SIMN predicted for this geometry before optimization, along with the SIMN calculated for the infinite cascade. Here the SIMN is plotted against the blade surface coordinate normalized by the axial chord, where positive values of s/c_{xl} correspond to the suction side of the blade and negative values correspond to the pressure side of the blade. The SIMN distribution from the cascade simulation shows strong accelerations on both blade surfaces, with supersonic flow towards the blade trailing edge and oblique shocks in the upper passage. Obviously the initial geometry does not produce the correct pressure distribution. First, the acceleration over the leading edge suction side of the blade is too low, leading to low values of SIMN between x/c_{xl} = 0→0.3. Second, the shock structure is completely misrepresented as well. This geometry produces a very weak oblique shock followed by strong acceleration up to the trailing-edge fish-tail shock. The agreement along the

pressure side of the blade is better, but there is an obvious shift in the SIMN predictions. Finally, the stagnation point location for CFD-DP is in error by 3.8% of the blade chord.

During the optimization, the solution for the suction wall (near the pressure side of the blade) converged very quickly, due to the favorable pressure gradient and the relatively small region of supersonic flow. However the optimization for the pressure wall proved much more difficult, since the shock structure shown in Figure 9 was extremely sensitive to changes in the wall geometry. In addition another problem that arose during the optimization was that a separation bubble appeared in the region of high curvature on the pressure wall. As the optimization routine changed the passage shape improving the SIMN, the size of the separation bubble increased slightly. Our initial approach to solve this problem was to manually create a new geometry based on the initial converged solution, with the bubble removed and a new wall surface along the dividing streamline, as shown in Figure 10. Iterations were continued with the new wall surface and the first version of the experimental apparatus was built to test the concept. Figure 11 presents the wall shape for this initial design, and Figure 12 shows the corresponding SIMN compared to that of the infinite cascade and the experimental measurements.

The experimental measurements show excellent agreement with both the cascade and double passage simulations, for the entire pressure surface and for the suction surface up to the shock. While the measured peak value for the SIMN matches the predicted values, following the peak SIMN the measurements indicate a strong normal shock instead of the weaker oblique shocks predicted in the simulation. This was not too surprising as similar shock structures were observed in the optimization procedure while converging to the initial design geometry. As a proof-of-concept, this first run geometry showed that the inverse design technique can be used to create an effective cascade flow around a turbine blade. Additional improvements were made to the optimization procedure in order to improve the agreement in the supersonic region of the blade suction surface.

4.2 Final Design

Since the initial cost function was based only on the blade SIMN, there was nothing in the optimization procedure to prevent flow separation on the outer wall surfaces. To remedy this a shear stress penalty was added to the cost function to prevent separation along the pressure wall surface:

$$\gamma_2 = \int_{\Gamma_{pwall}} ds \forall \tau_w \leq \tau_w^b \qquad (13)$$

where τ_w^b is a lower bound on the shear stress to ensure that the boundary layer does not tend toward separation. Furthermore, the wall shear stress along the blade surface was also included as a way of ensuring that the boundary layer had similar characteristics to the infinite cascade:

$$\gamma_3 = \int_{\Gamma_{blade}} \left| \tau_w - \tau_w^* \right| ds \qquad (14)$$

Thus the cost function was defined based on an inviscid property and a viscous one. In addition, a line search was implemented for the determination of c in Eq. 5 to expedite convergence.

To further improve the agreement in the supersonic region where the shock structure was extremely sensitive to the wall shape, several additional control points were added in the downstream region of the shock after the initial optimization had converged. While this added flexibility helped to refine the result, it was found that the shear wall penalty over-constrained the problem in the supersonic region on the suction side of the blade and it was initially not possible to obtain perfect agreement with the target pressure distribution. Experimental measurements for an intermediate wall shape showed that we were able to obtain the correct shock structure without separated flow, but the agreement on the entire suction surface was compromised slightly. In response to this the pressure wall separation penalty was relaxed to facilitate better agreement along the suction side of the blade. As mentioned earlier some intermittent separation was observed in the corner region during the final experiment, indicating that the values used for the wall separation penalty were probably not conservative enough.

The passage geometry resulting from the final optimization is shown in Figure 13, and the resulting pressure distribution is shown in Figure 14. Excellent agreement can be seen between the cascade prediction, the double passage prediction, and the measurements. The two computed cases overlap nearly perfectly, and the measurements agree very well with the computations, with the exception that the peak values are about 4% higher for the measurements. Figure 15 shows the calculated Mach number contours for both the double passage and the infinite cascade. The predicted Mach number contours match the cascade values very well for most of the passage, indicating that the agreement for the blade surface shown in Figure 14 is likely to extend through the region surrounding the blade as well. The accuracy of the predicted velocity field is confirmed with the PIV measurements which will be shown below.

5 Results: PIV Measurements

5.1 Upstream data

Measurements taken upstream of the blade were used to check flow uniformity and to provide inlet data for the turbulence intensity and dissipation rate. Profiles of the streamwise and cross-stream velocity across the inlet are shown in Fig. 16, for a location 0.47C downstream of the inlet. At this location the passage geometry begins at X = 0 and the passage width is 0.84C. The profile location and coordinate system orientation are shown in Figure 5. Note that in this coordinate system, U is the cross-stream velocity and V is the streamwise velocity upstream of the blade. The turbulence grid produces a slight change in both velocity components, with the same overall mass flow. The differences in mean velocity produced by the grid are small (<5% for U and <2% for V), and mean

15

velocity measurements in the downstream window closer to the blade show no difference when the grid is removed (not shown).

Profiles of the two-dimensional Reynolds stresses across the inlet are shown in Figure 17. It is important to note that the boundary layers are very thin, so these measurements represent only the freestream turbulence as indicated by the very small levels of the Reynolds shear stress. Without a turbulence grid, the turbulence intensity is small, although the contraction introduces substantial anisotropy and non-uniformity. The grid increases the Reynolds normal stresses by roughly a factor of 50-100 for the streamwise component and 20-50 for the cross stream component. Again the contraction introduces substantial anisotropy, with the cross-stream fluctuations 40 to 75% greater than the streamwise velocity fluctuations after the contraction for the high turbulence case. This anisotropy will be shown to persist throughout the passage.

For the high turbulence case the two-dimensional Reynolds stresses were used to approximate the turbulent kinetic energy using equation (7), and the dissipation rate was estimated with the LES method described above. Profiles of these values are shown in Figure 18 (a), and their evolution along the stagnation streamline in Figure 18 (b). For these normalizations an inlet average value of $U_\infty = 117$ m/s and $\varepsilon_0 = 35,000$ m^2/s^3 was used.

5.2 Velocity measurements around the blade

Contour plots of the mean velocity around the blade are shown in Figs. 19-21. Also shown is a contour plot of the mean velocity magnitude. Figure 22 shows a sparse field of mean velocity vectors (1 in 10) to provide a visual representation of the overall flow features. These figures show the strong acceleration of the flow through the passage, up to 3.6 times the inlet value. In the X-direction, the U-velocity is initially very small and it accelerates to supersonic in the passage. In the Y-direction, the V-velocity is initially close to U_∞ and it accelerates strongly in the $-Y$ direction, dropping to zero and then to more than twice U_∞ in the opposite direction. The stagnation point is located slightly to the right of the leading edge as indicated by the velocity magnitude contours.

The trailing edge shocks can be seen as sharp changes in U for the lower passage and sharp changes in V for the upper passage, since the fishtail shock at the trailing edge is primarily aligned perpendicular to U and V for the lower and upper passages respectively. Figure 21 also shows the mean velocity calculated with the CFD. The computed and measured values for the mean velocity agree very well with the exception that the measured values are slightly higher than the CFD everywhere. The region of intermittent flow separation in the upper passage corner can not be clearly identified from the mean velocity contours, as the minimum mean velocity in the corner is still close to 80% of U_∞.

5.3 Turbulence measurements around the blade

The Reynolds normal stress in the X-direction is shown in Figure 23. In this direction the mean velocity is nearly zero at the passage inlet, and accelerates to supersonic speed in the passage. In the lower passage the u-component fluctuating velocity drops significantly in the first part of the acceleration (to about 60% of its initial value), and then increases to almost the upstream value. While there is a jump in magnitude across the trailing edge shock, the region of influence is relatively thin, and after the shock u'^2 drops quickly to almost the upstream value. Study of the instantaneous vector fields shows that the shock position and shape are unsteady, so the increase in measured turbulence in the shock region is likely to be a consequence of the shock unsteadiness rather than an increase in freestream turbulence. The turbulence behavior in the upper passage is dominated by the high turbulence streak that originates in the separated region in the corner and convects downstream with the flow. Approaching the upper passage u'^2 decreases as the flow accelerates in a similar manner to the lower passage, and then it jumps significantly when it intersects with the high turbulence streak and remains high throughout the passage.

The Reynolds normal stress in the Y-direction is shown in Figure 24. In this direction the turbulence was initially lower than in the X-direction, due to the anisotropy created by the grid and the contraction. In the lower passage this fluctuating velocity increases slightly in the first half of the passage and then remains nearly constant until the shock. Again there is a jump in turbulence at the shock location followed by a near return to the pre-shock value. In the upper passage, the v-component fluctuating velocity is essentially constant in the first part of the acceleration and then it increases as it approaches the corner region. Like the u component, the v-fluctuations jump as they intersect the streak and remain high in the rest of the upper passage.

The combined changes in u and v fluctuating velocities show that the mean turbulent kinetic energy does not change significantly in the regions where there is no intermittent flow separation. Figure 25 shows contours of k calculated with equation (7) normalized by the inlet value. In the lower portion of the lower passage the turbulent kinetic energy does not change at all. This is the region that is close to what would be the effective suction side of the neighboring blade, and it is where both the acceleration and streamline curvature are the highest. Very close to the lower wall surface, k drops to 80% of its initial value. In the center of the lower passage the turbulent kinetic energy increases slightly, up to 20% higher than the value at the inlet. Shortly before the shock k increases up to 40% over the inlet value, and remains about the same after the jump in the shock. Near the pressure side of the blade there is a large region where k is less than 80% of the inlet value. Approaching the stagnation point k drops to 70% of the initial value at 10% chord away from the blade, and it continues to drop for as far as the measurements go (up to about 0.8 mm away from the blade surface, or 1.6% blade chord). In the upper passage k increases approaching the corner and then remains high.

The calculated dissipation rate normalized by the inlet value is shown in Figure 26. In the center of the lower passage, ε increases gradually to about 10 times the value at the inlet. In the region of the lower passage closer to the lower wall, where the acceleration is strongest, ε increases to more than 30 times its initial value. A similar increase is shown in the region approaching the stagnation point, and the maximum value for dissipation near the blade is also close to 30 times the initial value. One detail that may not be clear on the plots is that the location of the maximum dissipation rate near the blade surface is not aligned with the stagnation point, rather it is farther to the left on the suction surface where the acceleration and streamline curvature are very high. In the upper passage, ε shows similar behavior to the lower passage up to the separated region, where it rises sharply to more than 50 times its initial value and remains nearly constant through the rest of the passage.

The local turbulence intensity calculated with equation (8) is shown in Figure 27. In the lower passage the turbulence intensity contours look the same as the contours for the mean velocity, since the acceleration is strong while the changes in turbulence levels are relatively small. In the upper passage however the changes in turbulence due to the corner separation are much stronger in comparison to the mean velocity, so the turbulence intensity contours in the upper passage reflect the shape of the high turbulence streak shown in Figure 25. In the lower passage the turbulence intensity drops from 4.2% to 1.7% both before and after the shock. The drop in turbulence intensity occurs sooner near the lower wall surface due to the stronger acceleration there combined with the slightly lower values of k. In the upper passage the turbulence intensity reaches a maximum of 15% in the corner, and then drops in the upper passage back to 4.2%. Approaching stagnation the turbulence intensity increases as the local flow velocity goes down, reaching a maximum of 15% at the measurement point nearest stagnation. In the trailing edge region with the fishtail shock, the jump in turbulence intensity can be used to identify the shock location much more clearly then the mean velocity, since the location of peak velocity fluctuations corresponds to the mean location of the shock.

5.4 Streamline data

To better illustrate the development of the turbulence through the flow passage, we next show the evolution of several turbulence quantities along four selected streamlines shown in Figure 28. Streamlines a and b pass through the lower passage which we believe is most representative of the true turbine flow. Streamline c is the stagnation streamline, and streamline d passes through the upper passage and is affected by the presence of the intermittent separation bubble. The positions of the streamlines were determined using CFD results which closely matched the measured mean velocities. Figure 29 shows the evolution of the mean velocity magnitude and the fluctuating velocities along streamline a. Figure 29(b) shows the stresses in the original fixed coordinate system and Figure 29(c) shows them rotated in coordinates which are aligned with the streamline direction at each position. Figure 30 shows the same data for streamline b.

For streamline a, the U-velocity increases almost linearly up to S/C = 2 and then it tapers off slightly. The corresponding fluctuating velocity u' decreases as expected with a

18

positive acceleration in the X-direction, and then it increases gradually after S/C = 2 up to slightly less than the initial value. In the Y-direction the flow acceleration is initially in the opposite direction of the V-velocity, resulting in a positive production of v' which can be seen in Figure 29(b). Just before S/C = 2 the V-velocity becomes negative and therefore aligned with the acceleration, resulting in a negative production of v' which can be seen in the slight decrease in v' after S/C = 2. When the rms velocities are rotated into streamwise components the changes are much more subtle. As the flow accelerates in the streamwise direction, the streamwise fluctuations go down and the cross-stream fluctuations go up as would be expected in a nozzle flow. Towards the end of the streamline approaching the shock the streamwise fluctuations increase slightly while the cross-stream fluctuations remain constant. The lowest turbulence measurements exhibit an oscillation that is characteristic of peak locking effects. These oscillations occur in a region in the lower passage where the smallest values of turbulence were measured (in this case for u' only). This low-turbulence region was the only location where the measured fluctuating velocities correspond to pixel displacements less than 0.5 pixels.

Along streamline b, the flow shows a similar evolution as along streamline a with the added detail that the streamline passes through the trailing edge shock. Here the streamline curvature is lower than for a and the streamline also passes through the low-turbulence region near the pressure side of the blade. As with streamline a, the fluctuating velocity components increase and decrease as expected with the flow accelerations in both directions, although the slight increase in u' after S/C = 2.1 is not fully explained by the contraction analogy. Both rms velocity components show a jump at the trailing edge shock, while the u'-component shows the more severe change since the U-velocity is nearly perpendicular to the fluctuating shock location. The rotated velocity components also show the expected drop in the streamwise and jump in cross-stream fluctuations, and rotation also reveals a slight jump in the streamwise velocity fluctuations upstream of the shock.

Figure 31 shows similar data for the stagnation streamline. Here turbulence data are shown only in a fixed coordinate system because the streamline does not rotate through a large angle. The fluctuating velocity in the streamwise direction (in this case v') goes up as the flow decelerates approaching stagnation, and the cross-stream velocity (u') decreases as predicted by rapid distortion theory.

The data for streamline d in the upper passage are shown in Figure 32. This is the streamline that passes through the high turbulence region caused by flow separation in the upper passage corner. Here the separation has a strong influence on the turbulence components, which can be seen most clearly in streamwise coordinates as shown in Fig. 32(c). The streamwise and cross stream fluctuating velocities remain nearly constant until they reach the separated region, after which they both rise sharply. The higher statistical uncertainty in this region in the upper passage can be seen in the relative noise in the measurements after S/C = 2.7. The most pronounced increase in velocity fluctuations is in the cross-stream direction, and there is a slight decrease towards the end of the streamline.

6 Further Analysis and Model Comparisons

The data set is smooth enough that we are able to accurately resolve gradients in the mean velocity and turbulence quantities to directly evaluate terms in the Reynolds stress transport equations. The various terms in the turbulent kinetic energy transport equation are now being evaluated to understand the evolution of the turbulence and for comparison to models.

Various model calculations are now being done for the full three-dimensional geometry and using the measured inlet boundary conditions. The 2D grid was extruded and the grid points clustered to the end-wall for both the infinite cascade and the designed double passage. Unlike the 2D simulations, where 2-layer was involved along the blade surface, and wall-functions were utilized along the pressure-wall and suction-wall, 2-layer was invoked along all wall surfaces. Comparisons between the 2D simulations and the 3D simulations on the centerplane show excellent agreement. Further comparisons of the models with the turbulence measurements are underway.

Nomenclature

c	=	step size
c_{xl}	=	axial chord length
C	=	true chord length
C_s	=	Smagorinsky constant used in dissipation estimate, = 0.17
$\mathbf{E}$	=	set of governing equations
I	=	number of cost function components
j	=	global cost function
k	=	turbulent kinetic energy
k_{inlet}	=	turbulent kinetic energy measured at inlet, = 55 m^2/s^2
M	=	isentropic Mach number
P	=	pressure
$Re_{c,\,exit}$	=	Reynolds number based on blade chord and exit velocity
$Re_{c,\,inlet}$	=	Reynolds number based on blade chord and inlet velocity
s	=	blade surface coordinate
S	=	distance along a streamline
S_{ij}	=	instantaneous velocity gradient tensor
Tu	=	turbulence intensity, = $\sqrt{(2/3k)}/\sqrt{(U^2 + V^2)}$
u_s', u_n'	=	rms velocities in the streamwise and cross-stream directions
u_i, u_j	=	instantaneous velocity components
U_∞	=	measured mean velocity averaged across inlet, =117 m/s
$\mathbf{U}$	=	state variable vector
U, u'	=	local mean and rms velocities in the X-direction
V, v'	=	local mean and rms velocities in the Y-direction
X, Y	=	fixed Cartesian system used for measurements and calculations
y^+	=	non-dimensional wall unit

Greek

α = weight coefficient

β = scaling factor

Δ = perturbation in optimization, filter size for dissipation rate

ε = dissipation rate

ε_0 = average dissipation from measurements at inlet, = 35,000 m^2/s^3

φ = control variable

γ = cost function component

Γ = bound of surface integral

θ = angle between control point and reference location

τ_{ij} = sub-grid scale stress tensor

τ_w = wall shear stress

Abbreviations

CFD = computational fluid dynamics

IR = interrogation region for PIV processing

LES = large eddy simulation

PIV = particle image velocimetry

SIMN = surface isentropic Mach number

Inlet total pressure	2.6 x 10^5 Pa	Inlet Mach number	0.3
Inlet total temperature	295 K	Exit Mach number	1.7
Mass flow	0.64 kg/s	Inlet flow angle	0.0°
Blade chord	50 mm	Exit flow angle	127.0°
$Re_{c,\,inlet}$	6.6 x 10^5	$Re_{c,\,exit}$	2.4 x 10^6

Table 1. Geometric and flow conditions for experiment
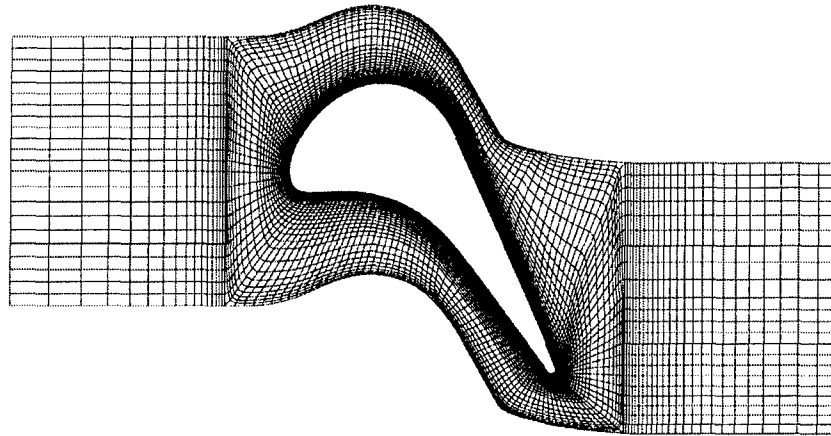
Figure 1. Computational grid used in infinite cascade simulations (not to scale)

to muffler

plastic walls

from
compressor

blade

windows

turbulence grid

nozzle

test section

0.327m
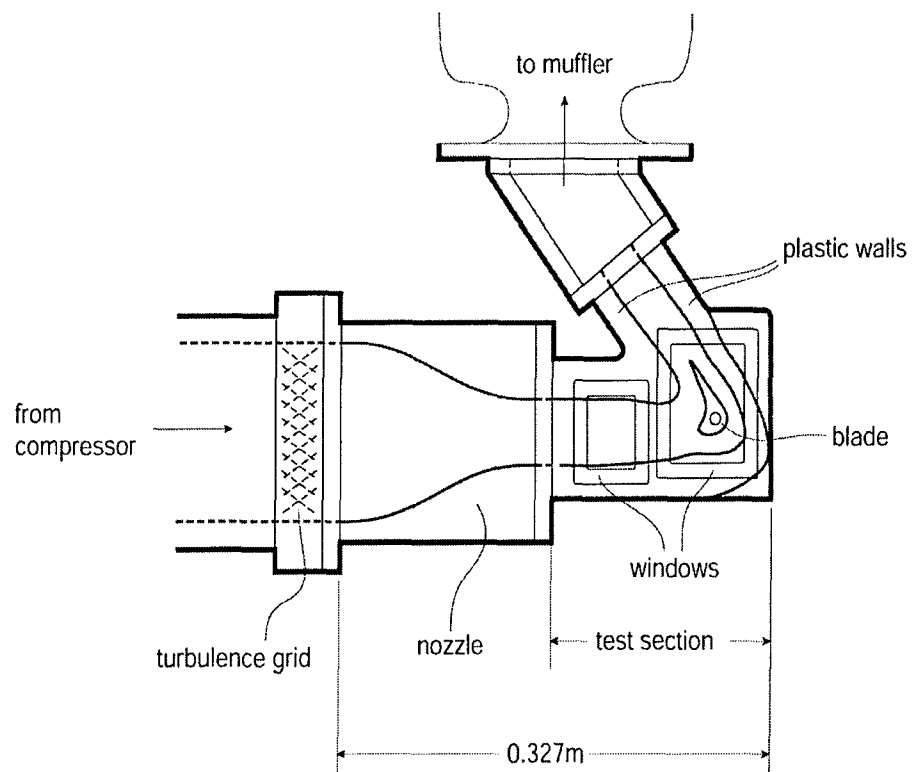
Figure 2. Wind tunnel test section schematic (not to scale)
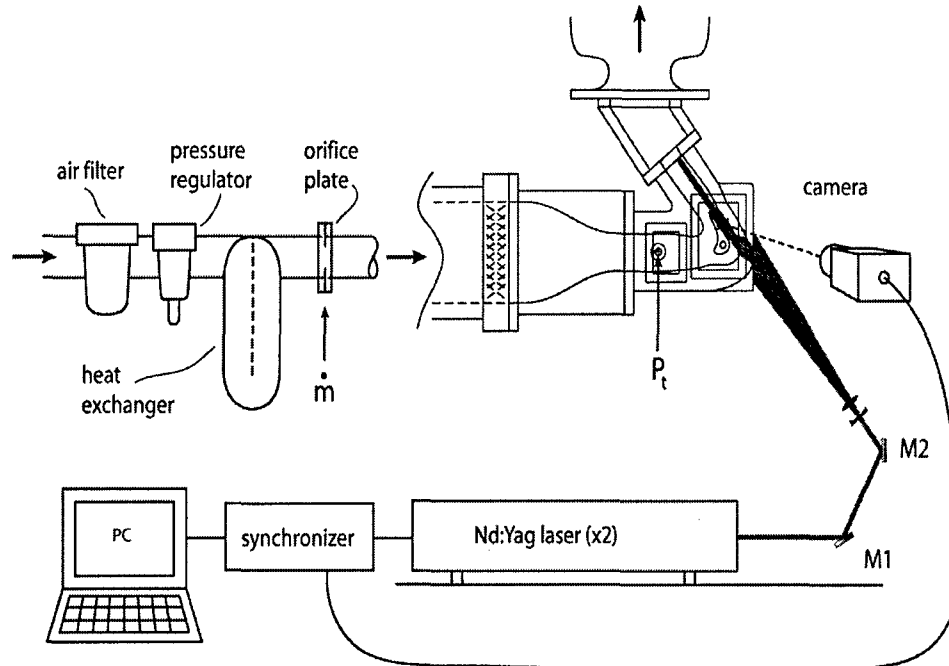
Figure 3. Upstream wind tunnel components and PIV setup (not to scale)
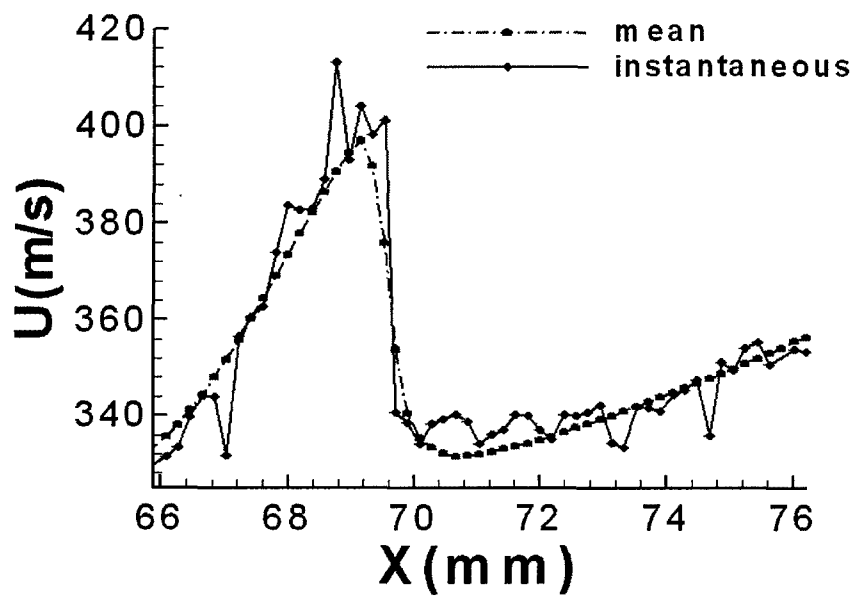
Figure 4. Mean and instantaneous velocity distribution across the trailing edge shock.
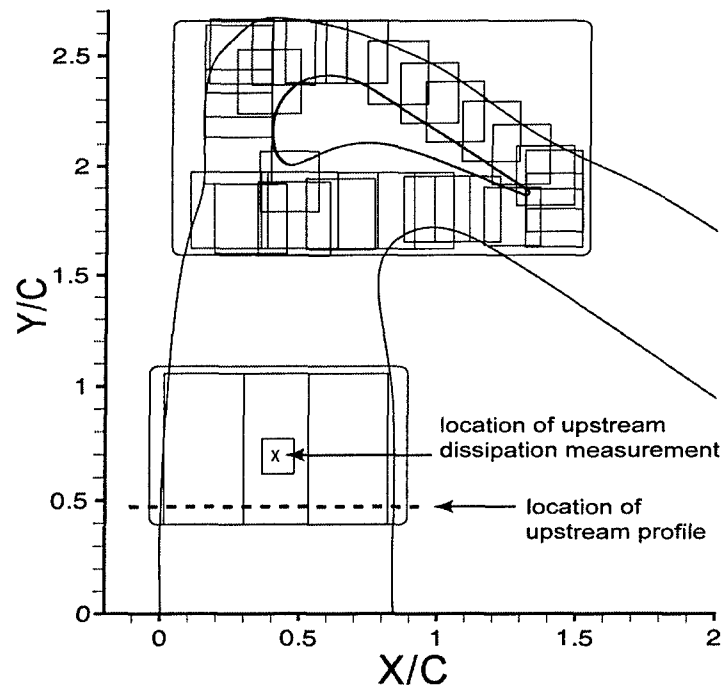
Figure 5. Measurement window location and coordinate system orientation (not to scale)
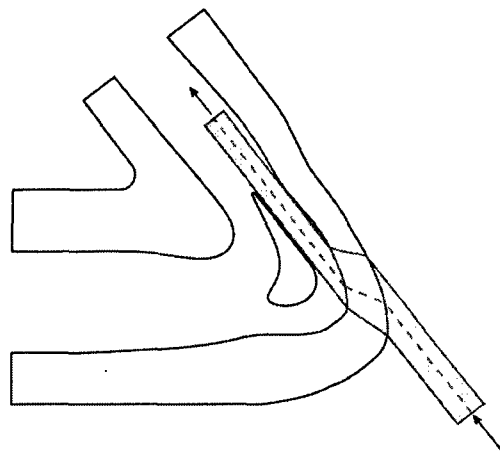
Figure 6. Example of shaped outer wall for optimal laser sheet access (not to scale)
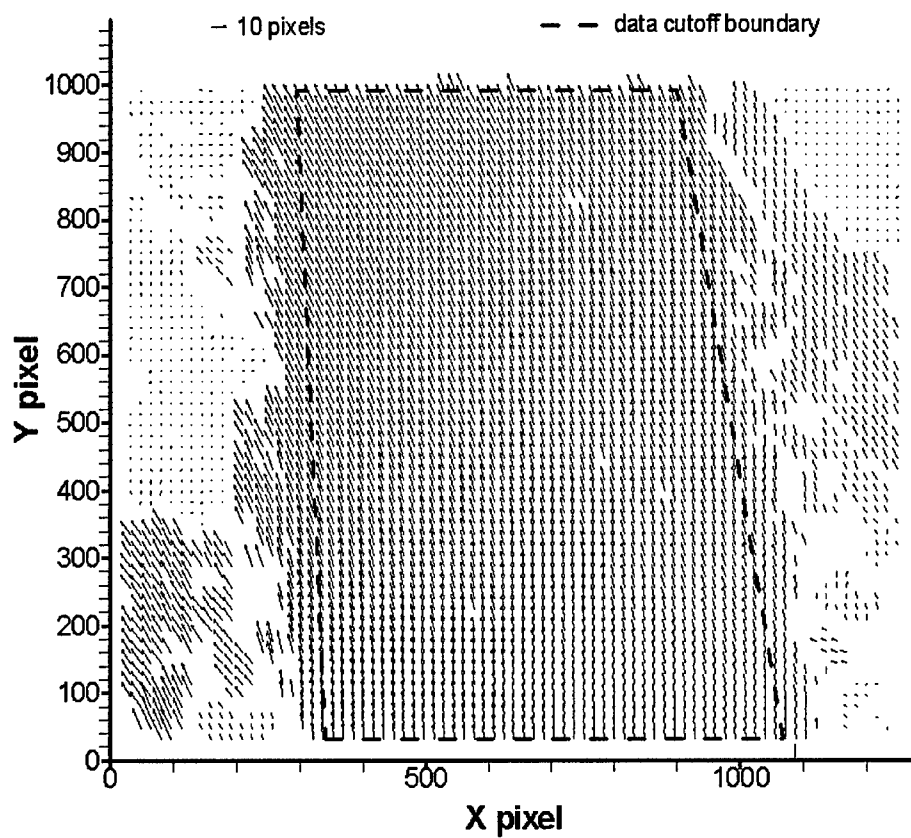
Figure 7. Sample validated vector field. In this case 10 pixels corresponds to a velocity of 155.6 m/s
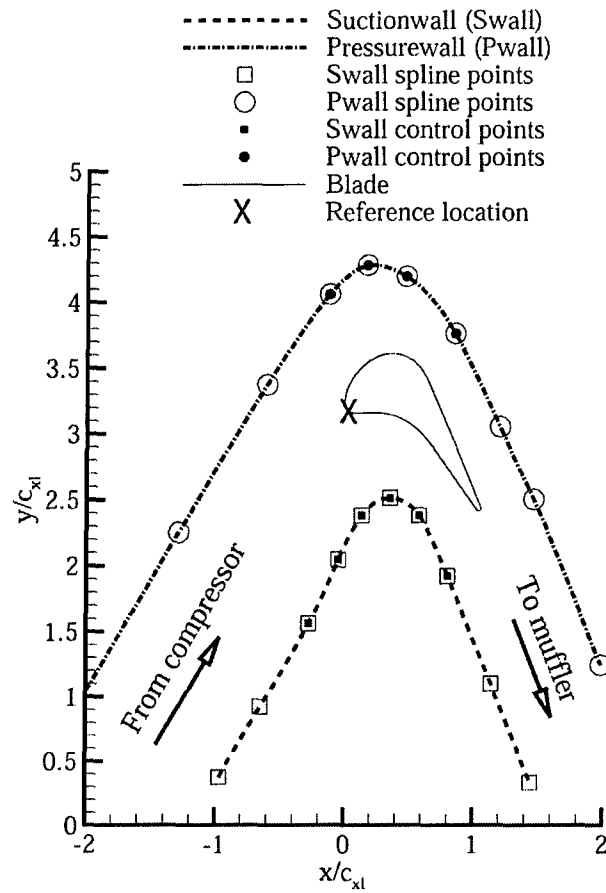
Figure 8. Initial geometry and control point locations
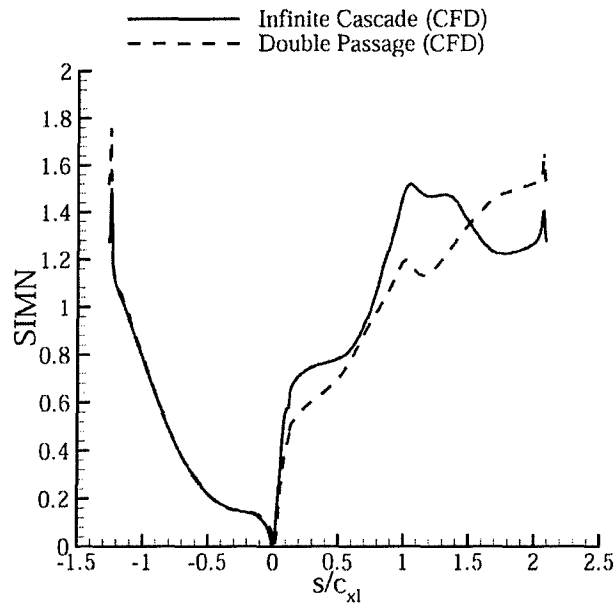
Figure 9. Predicted SIMN for infinite cascade and initial geometry (see Figure 8)
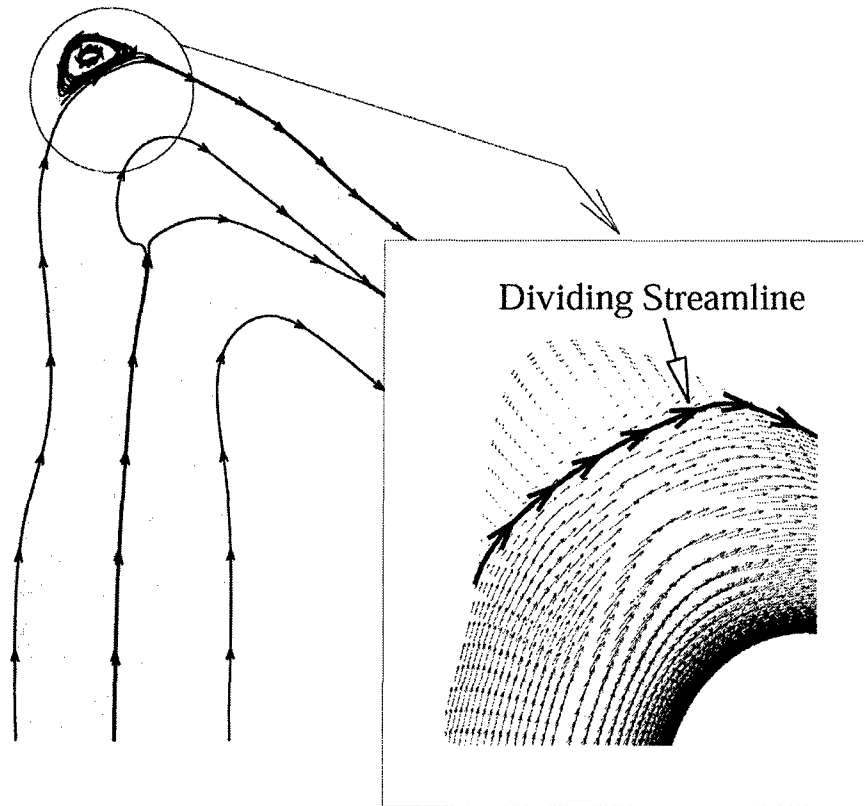
Figure 10. Separation along pressure wall and dividing streamline
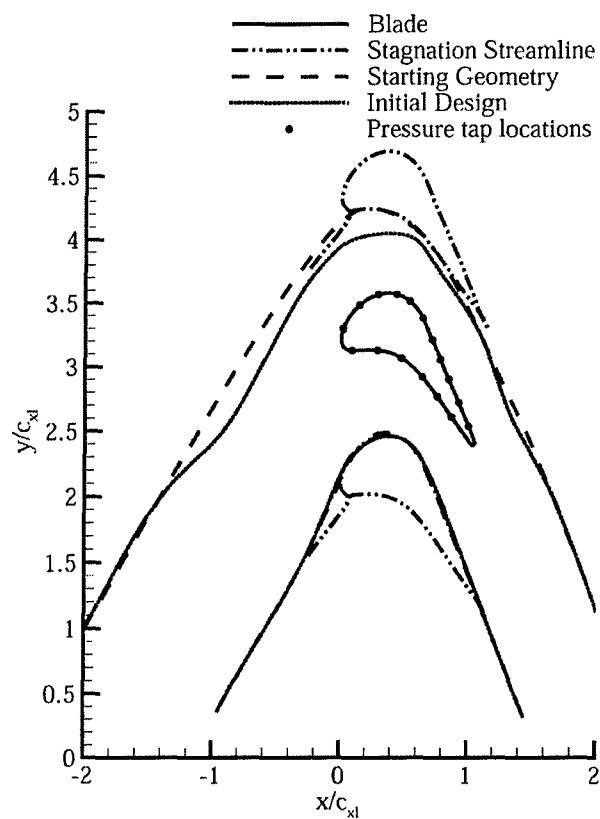
Figure 11. Initial and final wall geometries for the first design
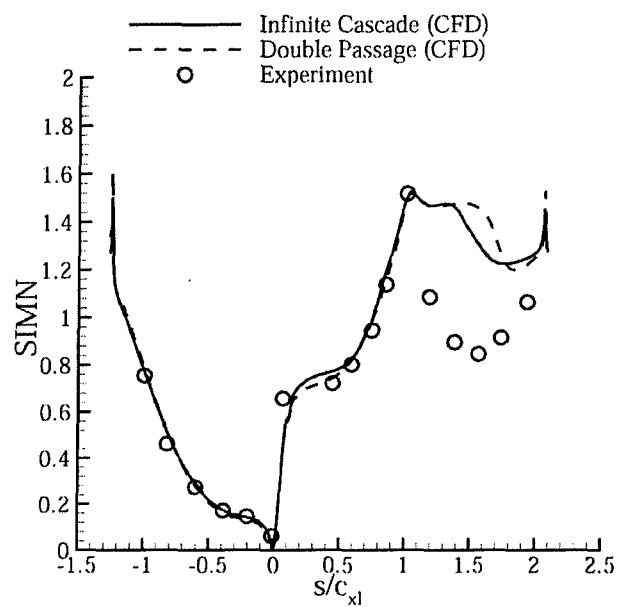
Figure 12. SIMN for the first geometry (see Figure 11)
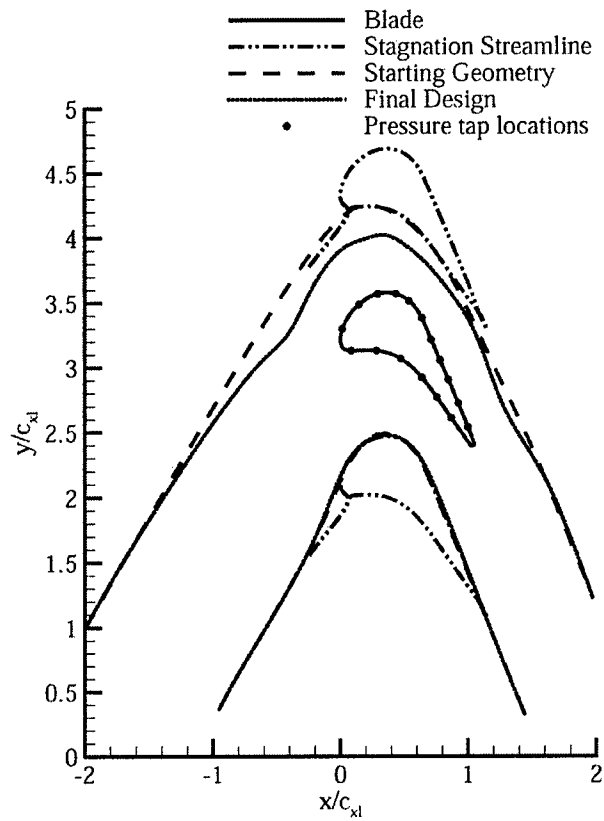
Figure13. Initial and final wall geometries for the final design
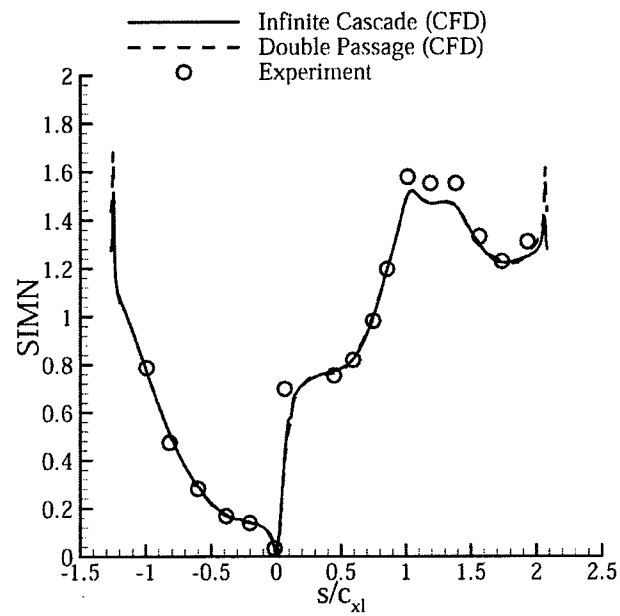
Figure 14. SIMN for the final design (see Figure 13)
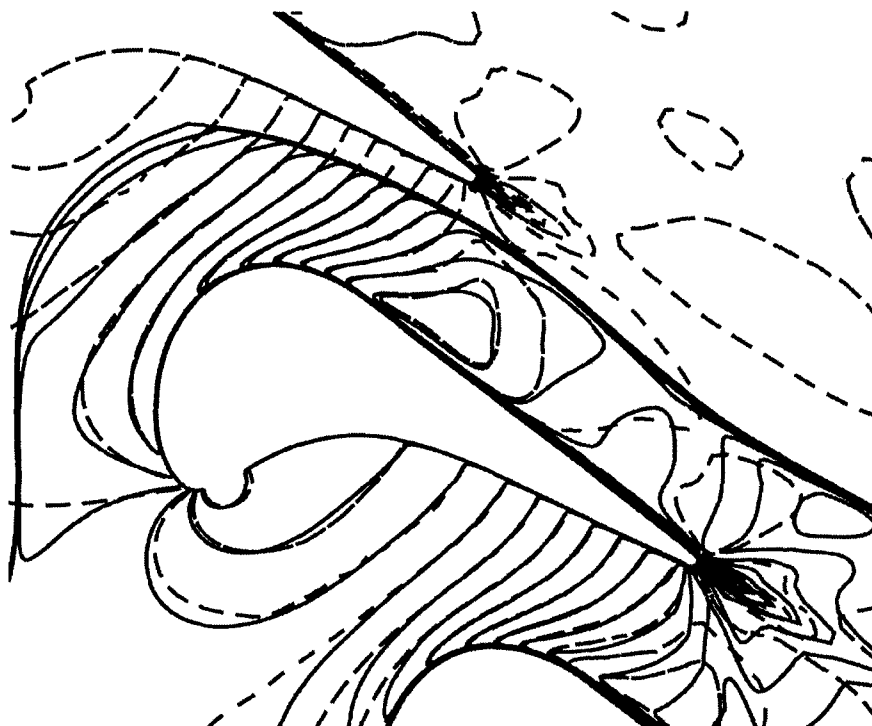
Figure 15. Mach number comparison between the calculated infinite cascade and double passage
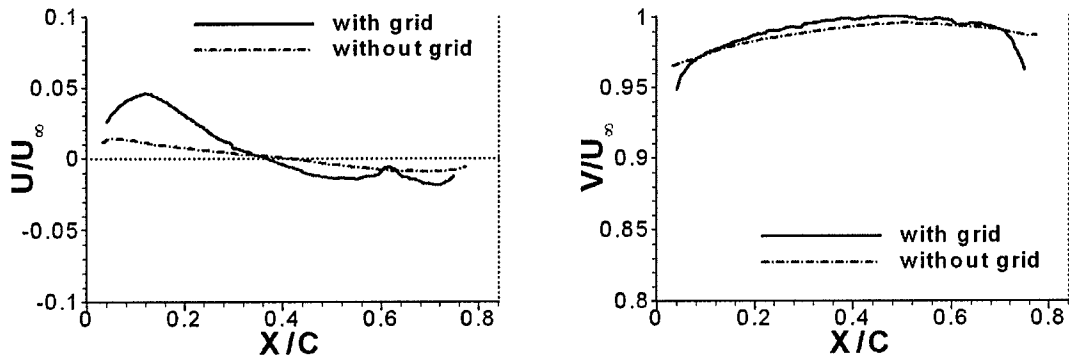
Figure 16. (a) U-component (cross-stream) mean velocity at inlet, and (b) V-component (streamwise) mean velocity at inlet. See Figure 5 for the profile location
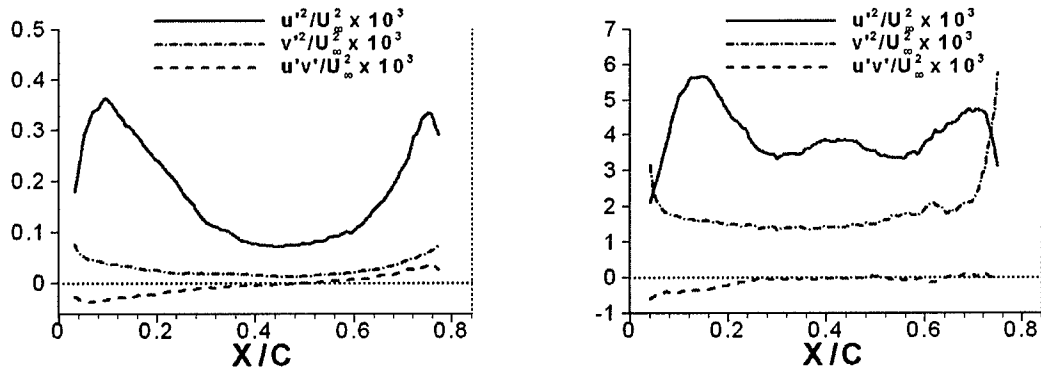
Figure 17. Reynolds stresses at inlet, (a) without turbulence grid, and (b) with grid. Note the differences in scale between the left and right figures
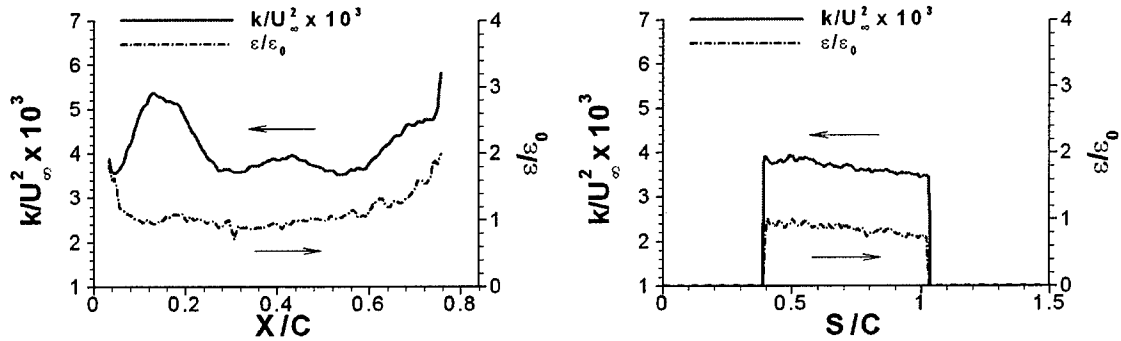
Figure 18. (a) Profiles of k and ε at passage inlet; (b) Streamwise variation of k and ε at upstream window, stagnation streamline
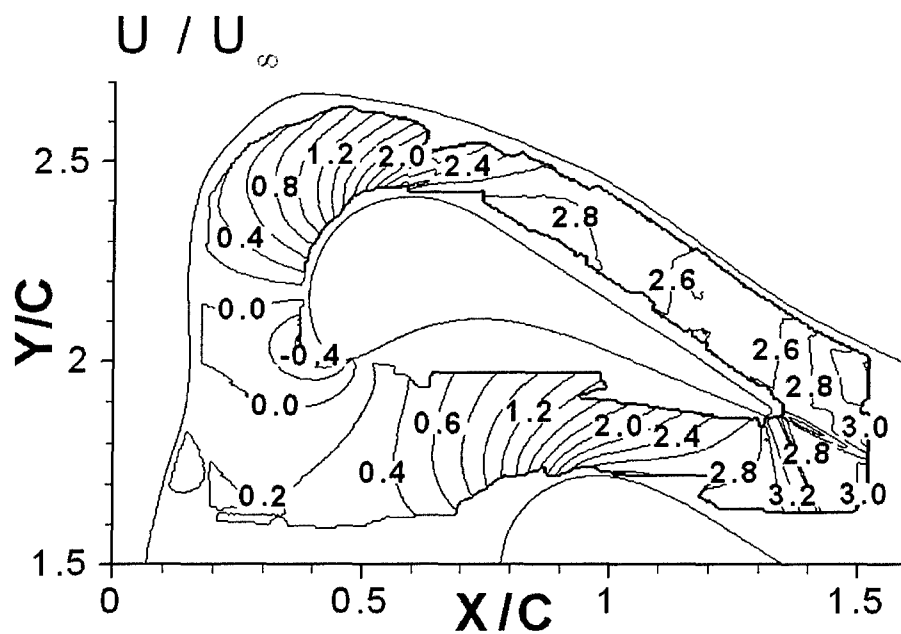
Figure 19. Mean velocity in the X-direction. Contour spacing is 0.2
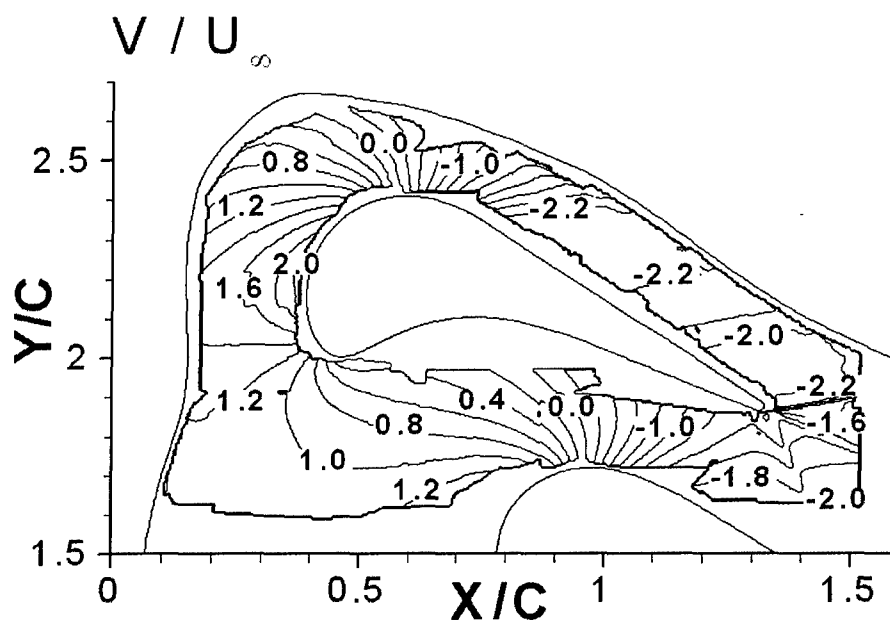
Figure 20. Mean velocity in the Y-direction. Contour spacing is 0.2

velocity magnitude / U$_\infty$
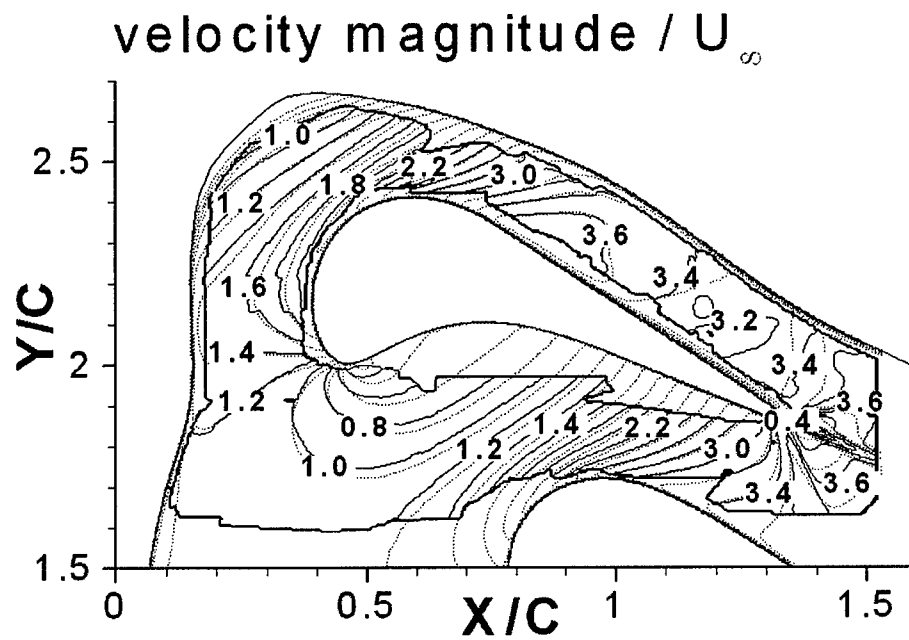
Figure 21. Mean velocity magnitude. Dotted lines are CFD, and contour spacing is 0.2
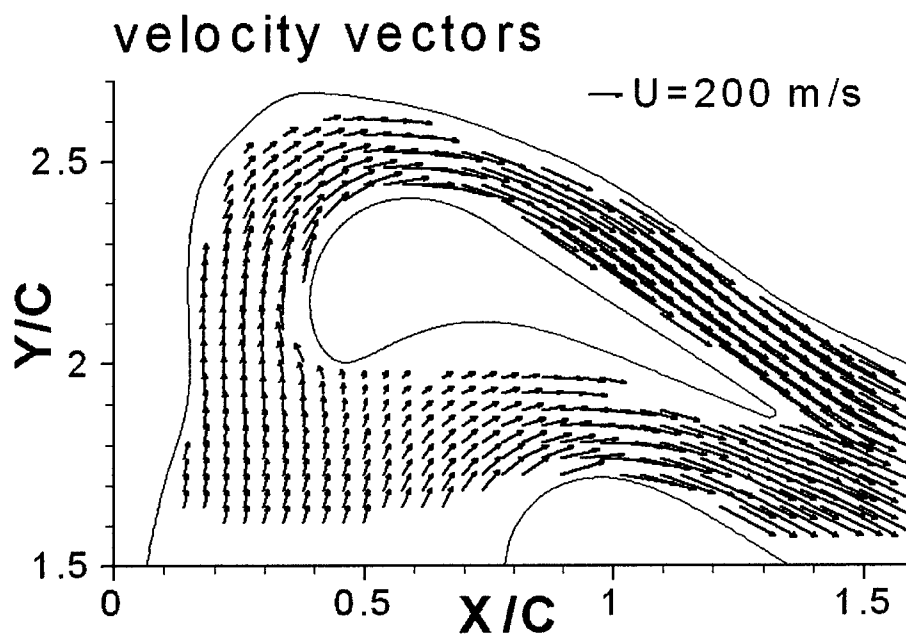
velocity vectors

Figure 22. Mean velocity vectors. Only 1 in 10 are shown
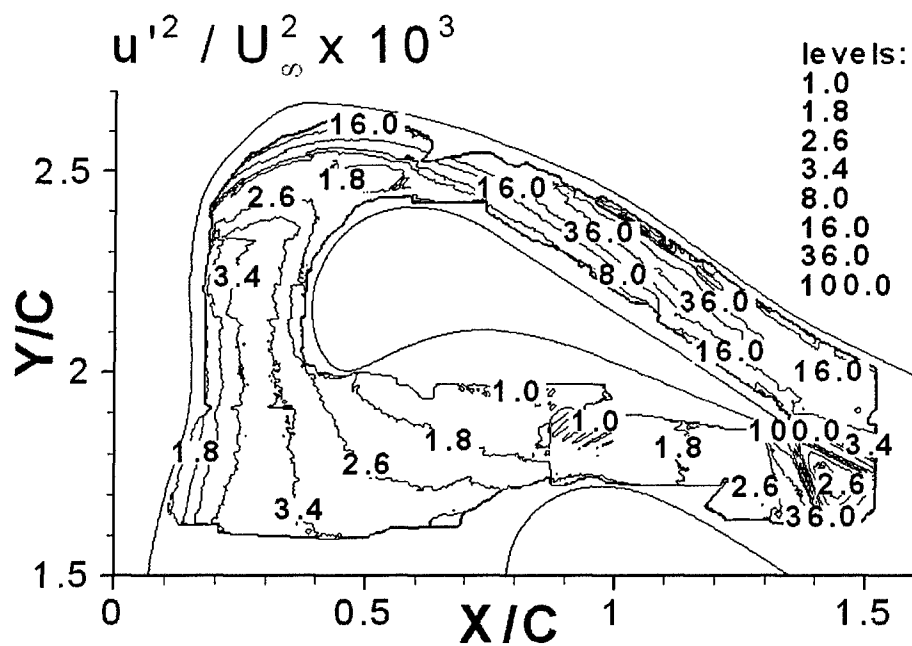
Figure 23. Normalized turbulence energy in the X-direction, u'^2 / U_∞^2
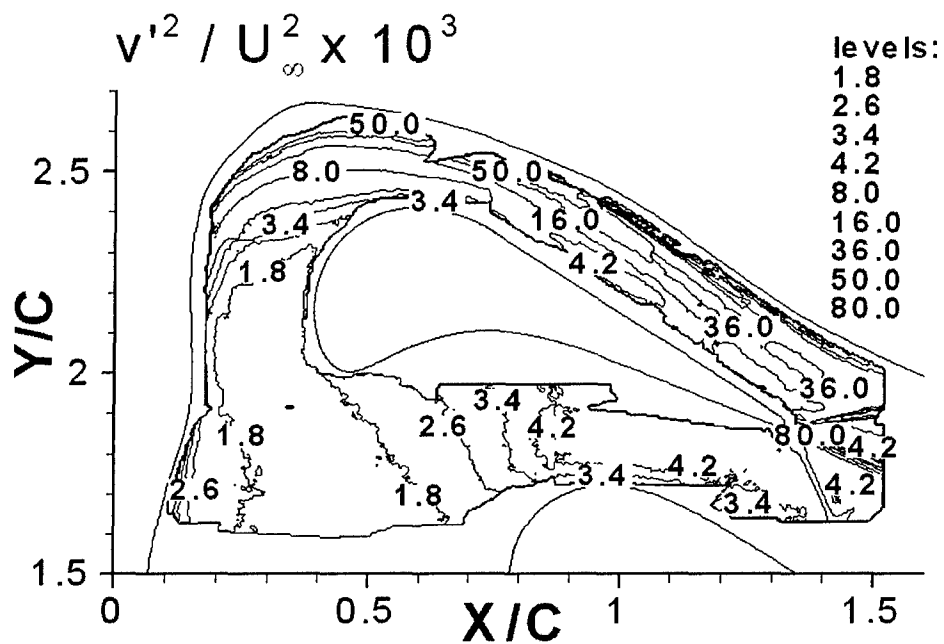
Figure 24. Normalized turbulence energy in the Y-direction, v'^2 / U_∞^2
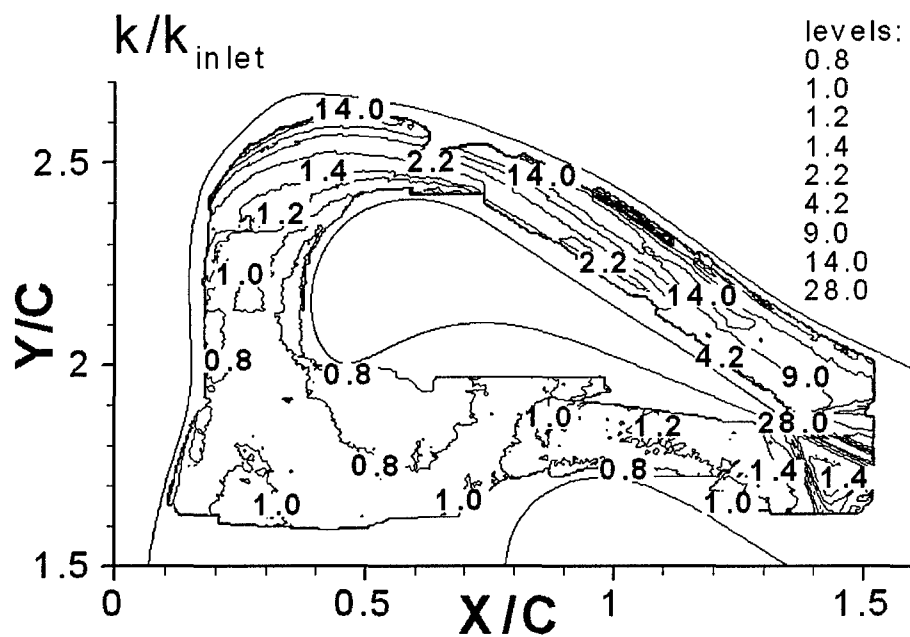
Figure 25. Normalized k around the blade
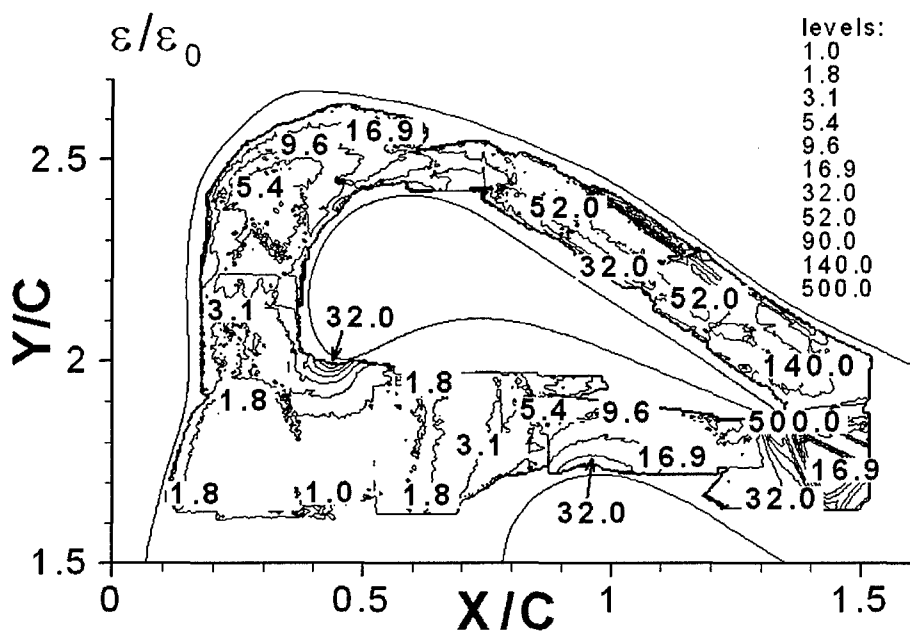
Figure 26. Normalized ε around the blade
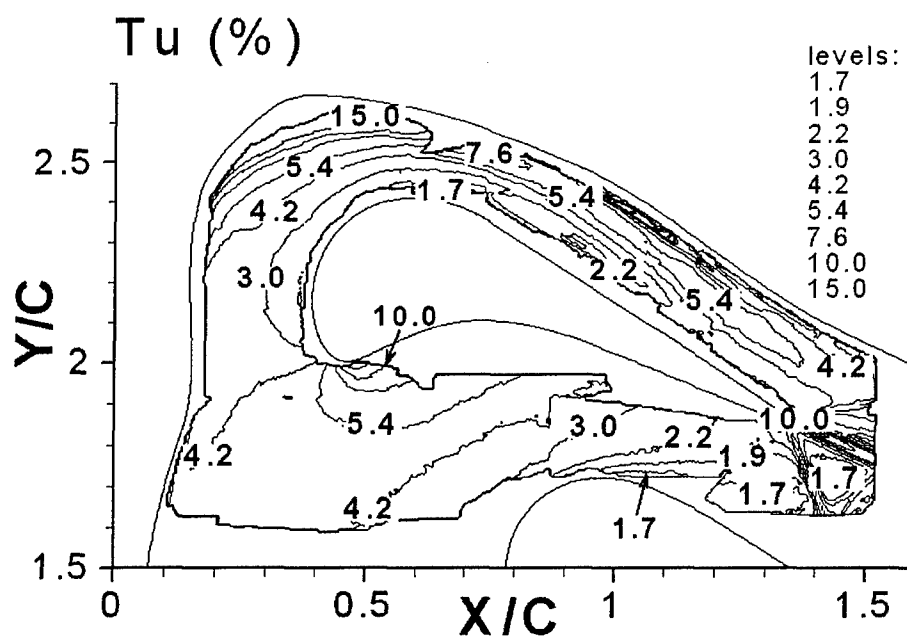
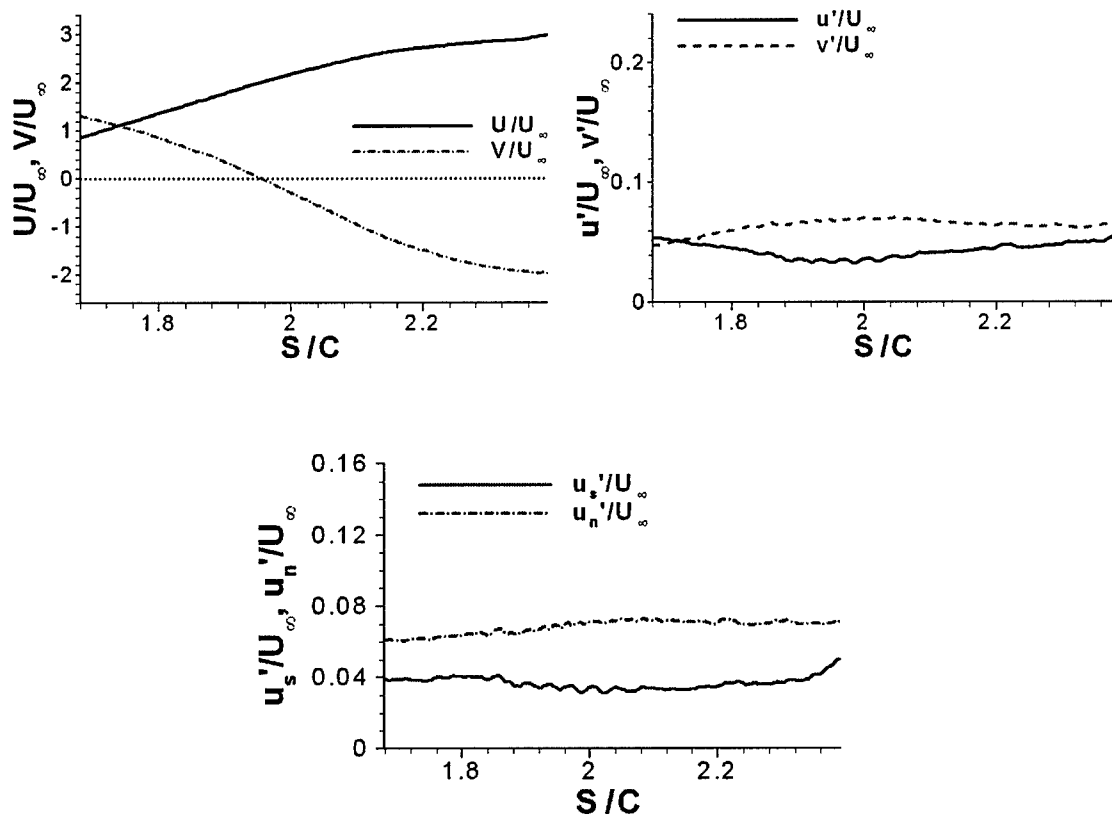Figure 27. Turbulence intensity contours
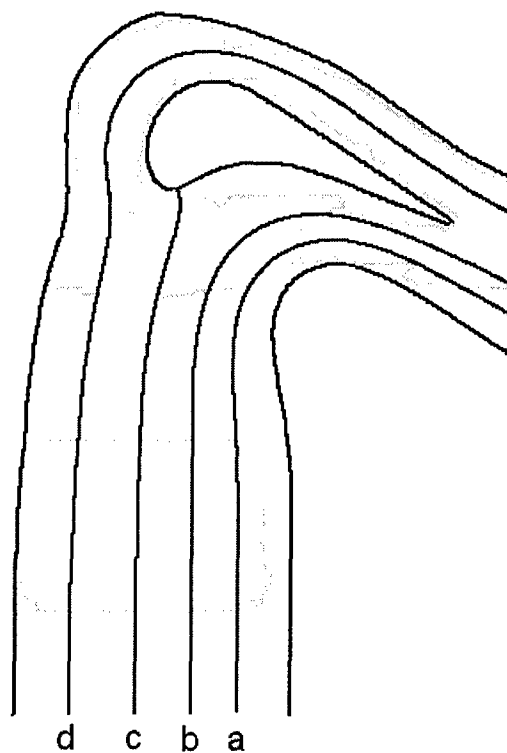
Figure 28. Streamline locations

Figure 29. (a) Normalized mean velocity components, (b) turbulence components, and (c) turbulence components in streamwise coordinates, along streamline a in the lower passage
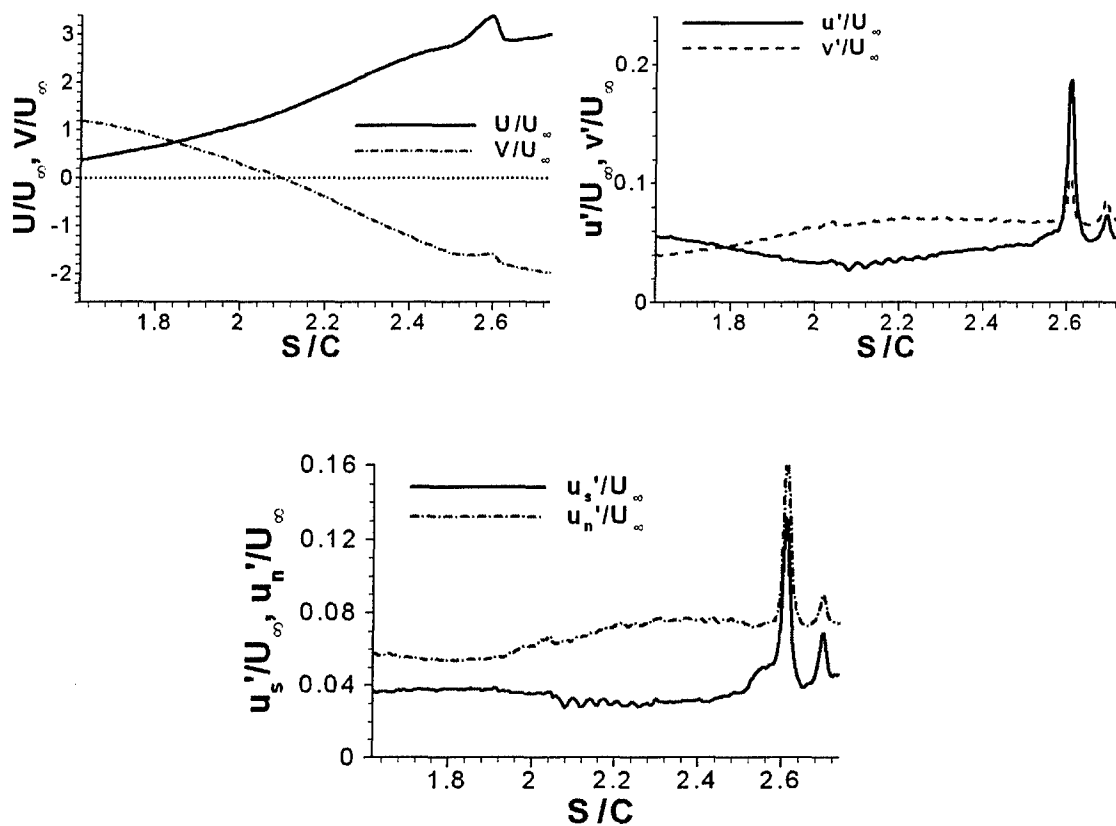
Figure 30. (a) Normalized mean velocity components, (b) turbulence components, and (c) turbulence components in streamwise coordinates, along streamline b in the lower passage
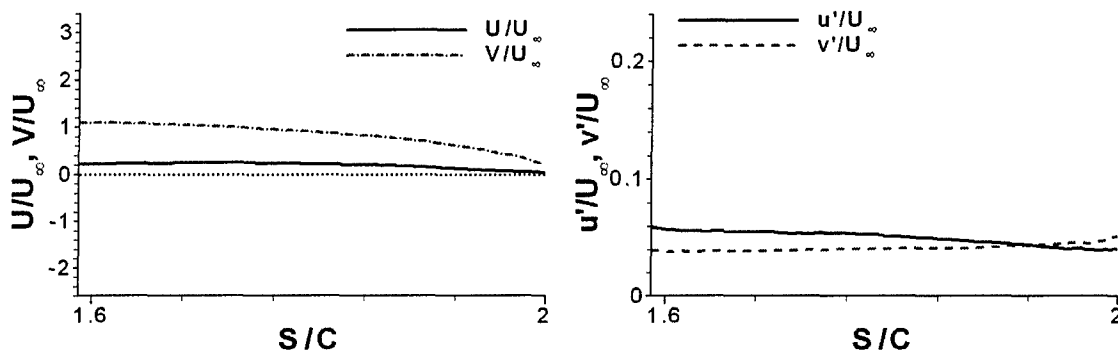

Figure 31. (a) Normalized mean velocity components, and (b) turbulence components along the stagnation streamline
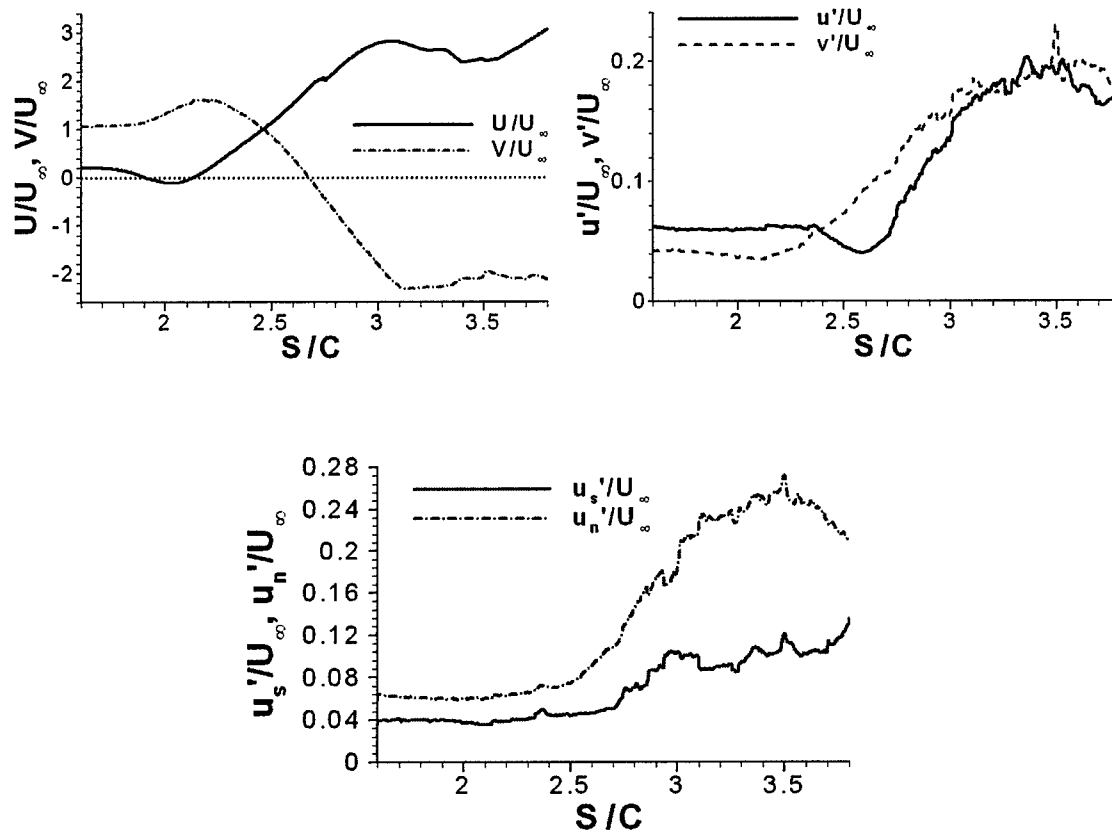
Figure 32. (a) Normalized mean velocity components, (b) turbulence components, and (c) turbulence components in streamwise coordinates, along streamline d in the upper passage

References

[1] STAR-CD Version-3.10, 1999, Methodology, Computational Dynamics Ltd.

[2] Medic, G., Durbin, P. A., 2002, "Toward Improved Prediction of Heat Transfer on Turbine Blades", Journal of Turbomachinery, v 124, pp. 187-192.

[3] Westerweel, J., 1997, "Fundamentals of Digital Particle Image Velocimetry." Meas. Sci. Technol., 8, pp. 1379-1392.

[4] Han, D., 2001, "Study of Turbulent Nonpremixed Jet Flames Using Simultaneous Measurements of Velocity and Ch Distribution," Technical Report TSD-134, Stanford University.

[5] Sheng, J., Meng, H., and Fox, R., 2000, "A Large Eddy PIV Method for Turbulence Dissipation Rate Estimation," Chemical Engineering Science, 55, pp. 4423-4434.

[6] Vicharelli, A., and Eaton, J. K., 2005, "Turbulence Measurements in a Transonic Two-Passage Turbine Cascade," submitted to Experiments in Fluids.

Appendix A – Personnel Supported During Duration of Grant

Greg Laskowski	Graduate Student, Stanford University
	PhD 2004, now at Sandia National Laboratories, California
Amanda Vicharelli	Graduate Student, Stanford University
	Ms 2004, continuing PhD
Christopher Elkins	Senior Research Engineer, Stanford University
Simon Song	Research Associate, Stanford University
	Asst. Professor, Hanyang University, Korea
Gorazd Medic	Engineering Research Associate, Stanford University
Paul A. Durbin	Professor, Stanford University
John K. Eaton	Professor, Stanford University

Appendix B – Publications

Laskowski, G., Vicharelli, A., Medic, G., Elkins, C., Eaton, J., Durbin, P., "Inverse Design of and Experimental Measurements in a Transonic Turbine Cascade Model," J. of Turbomachinery, to appear July 2005.

Laskowski, G., 2004, "Inverse Design of a Turbine Cascade Passage & DNS of a Stationary and Rotating Serpentine Passage," PhD thesis, Department of Aeronautics and Astronautics, Stanford University.

Vicharelli, A., and Eaton, J. K., 2005, "Turbulence Measurements in a Transonic Two-Passage Turbine Cascade," submitted to Experiments in Fluids.